remote sensing

MDPI

Article

A Case Study on the Integration of Remote Sensing for Predicting Complicated Forest Fire Spread

Pingbo Liu [1,2] and Gui Zhang [1,*]

[1] College of Forestry, Central South University of Forestry and Technology, Changsha 410004, China; liupingbo@csuft.edu.cn
[2] College of Computer Science and Mathematics, Central South University of Forestry and Technology, Changsha 410004, China
* Correspondence: zgui@csuft.edu.cn

Abstract: Forest fires can occur suddenly and have significant environmental, economic, and social consequences. The timely and accurate evaluation and prediction of their progression, particularly the spread speed in difficult-to-access areas, are essential for emergency management departments to proactively implement prevention strategies and extinguish fires using scientific methods. This paper provides an analysis of models for predicting forest fire spread in China and globally. Incorporating remote sensing (RS) technology and forest fire science as the theoretical foundation, and utilizing the Wang Zhengfei forest fire spread model (1983), which is noted for its broad adaptability in China as the technical framework, this study constructs a forest fire spread model based on remote sensing interpretation. The model improves the existing model by adding elevation an factor and optimizes the method for acquiring certain parameters. By considering regional landforms (ridge lines, valley lines, and slopes) and vegetation coverage, this paper establishes three-dimensional visual interpretation markers for identifying hotspots; the orientation of the hotspots can be identified to simulate the spread of the fire uphill, downhill, in the direction of the wind, left-level slope, and right-level slope. Then, the data of Sentinel-2 and DEM were used to invert the fuel humidity and slope of pixels in the fire line areas. The statistical inversion data from pixels, which replaced fixed-point values in traditional models, were utilized for predicting forest fire spread speed. In this paper, the model was applied to the case of a forest fire in Mianning County, Sichuan Province, China, and verified using high-time-resolution Himawari-8 data, Gaofen-4 data, and historical data. The results demonstrate that the direction and maximum speed of fire spread for the fire lines in Baifen Mountai, Jiaguer Villageand, Muchanggou, Xujiabaozi, and Zhaizigou are uphill, 16.5 m/min; wind direction, 17.32 m/min; wind direction, 1.59 m/min; and wind direction, 5.67 m/min. The differences are mainly due to the locations of the fire lines, moisture content of combustibles, and maximum slopes being different. Across the entire fire line area, the average rate of increase in the area of open flames within one hour was 3.257 hm^2/10 min (square hectares per 10 min), closely matching the average increase rate (3.297 hm^2/10 min) monitored by the Himawari-8 satellite in 10 min intervals. In contrast, conventional fixed-point fire spread models predicted an average rate of increase of 3.5637 hm^2/10 min, which shows a larger discrepancy compared to the Himawari-8 satellite monitoring results. Moreover, when compared to the fire spot monitoring results from the Gaofen-4 satellite taken 54 min after the initial location of the fire line, the predictions from the RS-enabled fire spread model, which integrates remote sensing interpretations, closely matched the actual observed fire boundaries. Although the predictions from the RS-enabled fire spread model and the traditional model both align with historical data in terms of the overall fire development trends, the RS-enabled model exhibits higher reliability and can provide more accurate information for forest fire emergency departments, enabling effective pre-emptive measures and scientific firefighting strategies.

Keywords: forest fire spread; Wang Zhengfei model; remote sensing; prediction

check for updates

Citation: Liu, P.; Zhang, G. A Case Study on the Integration of Remote Sensing for Predicting Complicated Forest Fire Spread. *Remote Sens.* **2024**, *16*, 3969. https://doi.org/10.3390/rs16213969

Academic Editor: Melanie Vanderhoof

Received: 14 August 2024
Revised: 19 October 2024
Accepted: 23 October 2024
Published: 25 October 2024

Copyright: © 2024 by the authors. Licensee MDPI, Basel, Switzerland. This article is an open access article distributed under the terms and conditions of the Creative Commons Attribution (CC BY) license (https://creativecommons.org/licenses/by/4.0/).

1. Introduction

Forests, the largest terrestrial ecosystems on Earth, are essential for maintaining global ecological balance, stabilizing the climate, conserving biodiversity, and providing resources crucial for human life. As human society evolves, the planet is witnessing a surge in extreme climates, resulting in a heightened frequency of forest fires globally. In February 2022, the Intergovernmental Panel on Climate Change released its report: with a global warming temperature of 1.5 °C, the world will face inevitable multiple climate hazards, and even temporarily exceeding this warming level will cause additional severe impacts, and China will be one of the most affected areas [1]. This means that the fire prevention situation is extremely serious in relation to the future.

Forest fires typically occur unexpectedly, spread quickly, and can lead to significant impacts on the environment, economy, and society. Forest fire fighting is recognized as a global problem. Forest fires in China predominantly occur in mountainous and hilly regions during the winter and spring seasons, when the weather is dry and vegetation is withered. The terrain in forested areas is highly varied, with overlapping peaks and deep ravines, which can easily create pronounced updrafts that trigger sudden changes in the wind's direction. This leads to the rapid spread of fire in multiple directions and the occurrence of extreme events, such as spot fires and explosive combustion, posing a severe threat to the safety of firefighting personnel. The timely and accurate evaluation and prediction of the progression patterns, particularly forest fire spreading speed in difficult-to-access areas, are essential for emergency management departments to proactively implement prevention strategies and put out fires using scientific methods.

The fundamental concept behind establishing a forest fire spread model involves mathematically processing various factors related to forest fire spread under simplified conditions. This approach identifies the relationships between these factors and the predicted outcomes. Using these relationships, the model characterizes the speed and other features of the temporal and spatial evolutions of forest fires, thereby predicting their subsequent spread. Currently, various forest fire spread models have been studied globally. Several classic forest fire spread models and their improved models are widely used, including the Canadian Forest Fire Danger Rating System [2], the McArthur model from Australia [3], the Rothermel model from the USA [4], and the Wang Zhengfei model from China [5]. The model from the Canadian forest fire risk prediction system focuses on the impact of slope on the spread speed, but its accuracy decreases in scenarios that deviate from experimental conditions. In Australia, the McArthur model proposed by Noble I.R. determines the fire spread speed solely by meteorological factors, such as wind speed and fire danger indexes, neglecting the impact of the combustibles themselves. The spread model proposed by Rothermel in the USA is based on the physical mechanism of the conservation of energy law, integrating wind speed, slope, and combustible information. While practical, this model requires many parameters that are difficult to obtain and has the stringent requirement of combustibles being in a uniform state, making it suitable only for predicting the spread speed in a single direction. The Wang Zhengfei model, developed in China, incorporates wind speed, slope, and types of combustibles [5], and is noted for its broad adaptability in China. However, the aforementioned traditional models often face significant limitations due to the restricted availability of fire location data and the difficulty of obtaining accurate parameters. More specifically, the areas where forest fires occur, such as in primary forests, often have complex and rugged terrains, making access and evacuation extremely difficult and dangerous for personnel. This results in significant challenges in obtaining the necessary parameters from these locations. These models typically rely on fixed-point measurements and rough estimates (e.g., using meteorological humidity data in place of ground-level fuel moisture), which leads to considerable discrepancies between the simulated results and the actual fire spread.

Remote sensing (RS) is an emerging technology that was developed in the early 1960s, based on aerial photography techniques. Since the launch of the first Earth observation satellite by the United States in 1972, RS technology has advanced rapidly. It is now widely

applied in fields such as environmental resources, hydrology, meteorology, geology, and geography, becoming a practical and advanced spatial detection technology. Meanwhile, the rapid advancement of satellite RS technology has overcome the high costs, complexity, and limitations of all-weather, all-directional, real-time monitoring associated with traditional forest fire monitoring methods, making RS an increasingly vital tool for surveillance [6–19]. In these RS applications, the application of the sixth version of the MODIS fire point identification algorithm reduced the daily global misclassification error to 1.2% [13], and the split window method of surface-temperature thermal infrared remote sensing inversion has been listed as a national standard by the Chinese Remote Sensing Technology Standardization Technical Committee [19]. But, RS technology has rarely been used for the prediction of fire spread. Fire emergency departments rely primarily on individual systems and video surveillance data to comprehend a fire scenario and base their firefighting strategies mostly on practical knowledge, rather than precise fire spread position and scientific fire trend analysis [20]. For accurate predictions, it is essential to have precise parameters or information for the models. However, these required parameters are often unknown or difficult to ascertain, and much of the data used are based on experience or historical records. Because of the unique capability of RS in the fast, and sometimes real-time, transmission of information, integrating RS data into fire prediction models is expected to significantly enhance prediction accuracy. This integration can provide critical fire spread data for relevant fire emergency departments to effectively and proactively deploy the required defense systems and manage fires using scientific methods.

Although remote sensing technology has not been directly integrated into forest fire spread models, the inversion technology of the key parameters of the model has been developed in other fields. Fuel humidity is one of the most critical factors affecting the spread of a fire, and experts have conducted some research on the remote sensing retrieval of vegetation humidity. Charles et al. and Carter found that reflectance sensitivity to water content is the highest, at the spectral bands of 1450, 1950, and 2500 nm within the 1300~2500 nm range [21,22]. Based on the correlation between spectral reflectance and vegetation water content, Deng et al. found good correlations between vegetation water content and spectral reflectance in the visible red-light band (620~700 nm) and near-infrared bands (800~1350, 1600~1950, and 2200~2400 nm) [23]. The angle slope index, proposed by Khanna et al., uses the geometric shape of the spectra across three consecutive bands to describe the relationships among these spectra, thus detecting not only the reflectance values of any band, but also the relationships between the bands [24]. The range of wavelengths affected by water's refraction and absorption spans approximately several-hundred nanometers [22,25], with strong correlations between individual bands in spectral imagery. The relationship of wavelengths between bands is as significant as the reflectance in the spectral data, under which premise the angle slope index is expected to more accurately represent the relationship between the spectral reflection and water content. Based on the angle slope index, a new leaf equivalent water thickness (LEWT) inversion model was developed by Lei et al. [26] using the improved distance projection ratio index (DPRI2), which in turn was used to invert the canopy equivalent water thickness (CEWT). Deng et al. [23], through improvements to the original angle slope index, proposed two, new, angle slope indices, the near-infrared angle normalized index (NANI) and the near-infrared angle slope index (NASI), which enhanced the accuracy of the inversion of the vegetation water content. It was shown that the linear regression model established with the ANIR index exhibits the highest fit, with a coefficient of determination of 0.791 and an RMSE of 0.047.

Slope is the degree of inclination of the local surface in space, and its magnitude directly affects the spread speed of forest fires, making it an important factor for studying forest fire spread. The digital elevation model (DEM), as one of the core databases of the Geographic Information System (GIS) spatial database, is fundamental for conducting two-dimensional spatial simulations of terrain and generating topographic maps. Therefore, a reasonable slope and aspect algorithm is essential for terrain analysis models. Currently, the

mainstream methods for extracting terrain information based on the DEM include six types: the second-order differential method, frame differential algorithm, third-order unweighted differential algorithm, third-order inverse-distance-squared weighted differential algorithm, third-order inverse-distance weighted differential algorithm, and simple differential algorithm [27–29]. Hao et al. [30], based on the DEMs of three different terrains, calculated the slope and aspect using six methods, and observed that the third-order differential series algorithms were quite applicable. The frame differential algorithm performed well in the Dongjiang Basin and the source of the Yellow River. Chen et al. [31], using the loess hilly gully region as a case study, studied the applicability of six slope extraction algorithms, using the standard deviation, maximum value, and slope grading area data extracted by the six different algorithms as statistical indicators, and employed one-way analysis of variance to explore the scope of application of the six algorithms. It was found that the third-order inverse-distance total difference and third-order inverse-distance-squared total difference algorithms worked well in the loess hilly gully region. Li et al. [32] used a DEM generated from a 1:10,000 topographic map as the study object, applied six algorithms to extract the slope and aspect values, and analyzed the algorithms suitable for the study area by comparing maximum values, mean errors, and cumulative absolute deviations, which provided a reference for practical work based on the conclusions drawn. Jiang et al. [33] using Qingdao City in Shandong Province as a case study, calculated the slope of the study area using six different algorithms, and statistically analyzed and calculated the slope matrices extracted using the different methods. The third-order differential series algorithm was found to have the highest accuracy and the lowest probability of extreme cases, being quite stable; among them, the third-order inverse-distance-squared total differential and third-order inverse-distance weighted differential algorithms exhibited the highest accuracy under various statistical indicators. Meanwhile, the simple differential, second-order differential, and frame algorithms show various degrees of bias and extreme cases under different statistical indicators.

The objective of the present paper is to evaluate the effectiveness of using RS data to improve fire spread predictions. By combining high-resolution satellite RS data, advanced interpretation technology, and an improved Zhengfei Wang forest fire spread model, the speed and area of forest fires spread are determined. The enhanced accuracy and reliability of the RS-enabled forest fire spread model are demonstrated.

2. Study Area and Data

2.1. Study Area

A forest fire that occurred in Mianning County (referred to as the Mianning fire in this paper) in Sichuan Province in China in April 2021 was used to compare the accuracy of the RS-enabled forest fire prediction. Mianning is located in the northeastern part of the Liangshan Yi Autonomous Prefecture, between the latitudes of 28°5′N and 29°2′N, and longitudes of 101°38′E to 102°19′E, as shown in Figure 1. Mianning County has a forest cover rate of 34.7%, which is rich in different species, including a total of 140 families, 341 genera, and 608 species of trees, shrubs, and herbaceous plants. It is situated in the middle of the Hengduan Mountains and features a complex terrain and significant elevation differences, with a high mountain canyon area that fosters a unique dry–hot valley climate. The time from March to May every year is the dry–hot season. In the three months before the arrival of the main southwest monsoon in June, it is both dry and hot, making it highly susceptible to forest fires. Once a forest fire occurs in such a place, it is often on a high-altitude region with a steep terrain, and the wind direction on the mountain can change abruptly, making firefighting dangerous and arduous due to the interplay of monsoons, mountain winds, and valley winds with high-altitude airflows. Therefore, the real-time and accurate remote sensing monitoring of forest fires is urgently and vitally important for guiding emergency fire responses and scientific firefighting efforts.

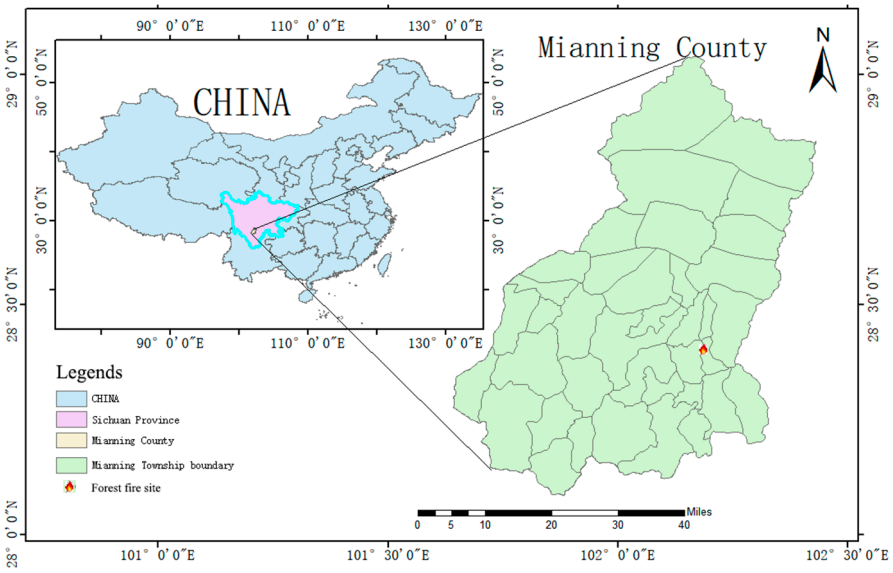


Figure 1. Forest fire area in Mianning County, Sichuan, in April 2021.

Based on the reliable resources from the historical reports of the People's Government of the Liangshan Yi Autonomous Prefecture and publicly available research papers, the Mianning forest fire started on 20 April 2021. The majority of the fire area consisted of primary forests, with the vegetation cover exceeding 80%, primarily composed of eucalyptus and other broadleaf forests. The area features crisscrossing ravines and steep mountain slopes. Some sections are made up of cliffs and are difficult to access, characterizing a typical high mountain canyon terrain. Figure 1 shows the area where the fire occurred. The Mianning fire has been classified as a major forest fire case in China [34].

Because of the challenges faced when trying to put out this fire, we consider the Mianning fire a good example to evaluate the accuracy for the RS-enabled forest fire prediction model.

According to the historical records in the literature, on the night of 23 April 2021, the fire site was suddenly impacted by strong winds with a force of 8 on the Beaufort scale (as reported by the on-site meteorological data). A sudden spot fire broke out on the southern side of the western line of the original fire, which was beyond the range that could be controlled. This triggered a new fire on the northern side of the Tuobie Mountain Ridge and near the western side of Baifen Mountain, creating a new fire site. The fire expanded rapidly, spreading south and north, merging with the original fire site. By 24 April 2021, the burned area had expanded significantly to the north and northwest, crossing Baifen Mountain and spreading toward Jiaguan Village. Two light-blue smoke columns, with particularly noticeable growth, were clearly visible near the eastern side of Baifen Mountain. The overall shape of the fire was "L"-shaped, measuring 5.8 km in length from north to south, 3.5 km in width from east to west, covering an area of approximately 9.55 km^2.

On 24 April 2021, the fire intensified significantly, with unusual growth, making it a good fire case for evaluating the forest fire spread model simulation, particularly for complicated fire prediction scenarios. In this paper, T03:45 (Universal Time) on 24 April 2021 was selected as the starting time node of the spread simulation.

2.2. Data

Multispectral data from Sentinel-2 were selected to estimate the moisture content of combustibles, while Himawari-8 and Gaofen-4 captured temperature anomalies. Data from Sentinel-2 were downloaded from the European Space Agency (ESA) Copernicus Data Centre (https://dataspace.copernicus.eu), accessed on 2 March 2023. Using Sen2Cor 2.5.5 software, L1C level products were radiometrically calibrated and converted into L2A level products. After preprocessing (mainly including geometric correction and atmospheric

correction), the Sentinel-2 images were projected as UTM Zone 48 WGS84 and resampled to a spatial resolution of 10 m. The full-scale observation data of Himawari-8 L1 NC (Network Common Data Format) were downloaded from the Japan Meteorological Agency (https://www.eorc.jaxa.jp/ptree/index.html, accessed on 2 March 2023) and reprojected with a bowtie correction. Data from Gaofen-4 were downloaded from the China Center for Resources Satellite Data and Application (https://www.cresda.com/zgzywxyyzx/index.html), accessed on 5 March 2023. Sentinel-2 satellite imagery and DEM data were used for orthorectification and precise geometric correction. The 30 m STER GDEM data were obtained from the Geospatial Data Cloud (https://www.gscloud.cn, accessed on 5 March 2023) for slope values. The 30 m resolution land cover type data (n48_25_2020lc030) were obtained from the National Geomatics Center of China. The selected bands of satellite imagery datasets used in the current study are shown in Table 1, and the experimental data information of the remote sensing imagery are shown in Table 2.

Table 1. Selected bands of satellite imagery datasets used in the current study.

Satellite	Sensor	Channel No.	Wavelength (μm)	Spatial Resolution (m)
Himawari-8	AHI	3	0.64	500
		4	0.86	1000
		5	1.60	2000
		6	2.30	2000
		7	3.90	2000
		8	6.20	2000
		14	11.20	2000
		16	13.30	2000
GF-4	IRS	6	3.80	400
Sentinel-2A	MSI	2	0.49	10
		3	0.56	10
		4	0.665	10
		8A	0.865	20
		11	1.61	20
		12	2.19	20

Table 2. Experimental data information for remote sensing imagery.

Satellite	Imagery	Application	Band
Sentinel-2	S2B_MSIL2A_20210424T034529_N9999_R104_T48RTS_20220305T083309.SAFE	Moisture interpretation of combustibles	4, 8, 11
		Smoke detection (true color composite image)	4, 3, 2
		Forest fire identification (false color composite image)	12, 11, 8A
Himawari-8	NC_H08_20210424_0340_R21_FLDK.06001_06001 NC_H08_20210424_0350_R21_FLDK.06001_06001 NC_H08_20210424_0400_R21_FLDK.06001_06001 NC_H08_20210424_0410_R21_FLDK.06001_06001 NC_H08_20210424_0420_R21_FLDK.06001_06001 NC_H08_20210424_0430_R21_FLDK.06001_06001 NC_H08_20210424_0440_R21_FLDK.06001_06001 NC_H08_20210424_0450_R21_FLDK.06001_06001 NC_H08_20210424_0500_R21_FLDK.06001_06001	Forest fire identification	7, 14
Gaofen-4	GF4_IRS_E103.0_N29.3_20210424 _L1A0000374570	Forest fire identification	6
	N48_25_2020LC030	Land cover	

The hourly meteorological data for Mianning County on 24 April 2021 were obtained from ERA5 (ECMWF Re -Analysis 5) hourly data on single levels from 1979 to the present. ERA5 represents the fifth generation of reanalysis data by the European Centre for Medium-Range Weather Forecasts, which provides numerical data for global climate and weather information over the past 40 to 70 years, as shown in Table 3. The software used included ENVI 5.3, ArcGIS 10.2, and MATLAB R2021a.

Table 3. Hourly meteorology for Mianning County on 24 April 2021.

Time (UTC)	Wind Direction	Wind Speed (m/s)	Relative Humidity (%)	Air Temperature 2 m (°C)
3:00	northward westward	1.23 0.81	62.58	15.97
4:00	northward westward	1.44 0.78	58.65	15.99
5:00	northward westward	1.48 0.54	46.37	19.02
6:00	northward westward	1.39 0.34	43.85	18.85
7:00	northward westward	1.22 0.10	39.77	19.24

3. Methodology

At the onset of the forest fire, satellite RS data capable of monitoring the fire were obtained and preprocessed for the inversion of the model parameters. In this study, Sentinel-2 satellite data were used to invert the moisture content of combustibles in the fire-affected area, 30 m STER GDEM data were used to invert the terrain's slope, and Gaofen-4 and Himawari-8 data were used to capture abnormal brightness temperatures. Based on the vegetation cover data for the fire area, instantaneous meteorological data (wind speed and wind direction), the moisture and slope information of each pixel along the fire line, and the speed of the potential fire spreading in potential directions were calculated. The maximum value in the possible spread direction was determined based on the statistical data for the spread speed. Under the premises of relatively stable meteorological data, minor changes in slope values, and consistent forest types, the area that the fire line can reach after a certain period based on the maximum speed was estimated, which could provide a basis for firefighting techniques. Finally, the fire spot pixels captured by Gaofen-4, Himawari-8 data, and historical archive data were used to validate the results of the RS-enabled fire spread predictions. The specific flow of the integration of RS and the fire spread model simulation is shown in Figure 2.

3.1. Model Selection and Improvements for Forest Fire Spread

To evaluate the benefits of integrating RS into forest fire spread models, a reliable model for predicting the specific areas susceptible to forest fires is essential. This study adopted the Wang Zhengfei forest fire spread model, which is widely used in China, as the basic framework. The model was modified to incorporate the elevation effect.

The fire spread prediction of the Wang Zhengfei model is shown in Formula (1).

$$R = R_0 K_S K_\omega / \cos\phi, \quad (1)$$

where R is the estimated fire spread speed (m/min), R_0 is the initial spread speed (m/min), K_S is the correction factor of type of combustibles, which is a constant that varies with time and locations, K_ω is the wind correction factor, $\cos\phi$ is the slope correction factor, and ϕ is the slope.

Mao et al. considered the combination of the terrain and wind direction to improve the slope influence factor, K_φ, and derived equations for five directions, upward slope, left-level slope, right-level slope, downward slope, and wind direction, thus enhancing the model's practical applicability [35]. Zhang and Liu incorporated the impact of combustible moisture on the fire spread speed [36], which improved the calculation of the slope correction factor and initial spread speed, resulting in a more accurate prediction of the fire spread speed. We considered the effects of the terrain and wind direction as well as the combustibles moisture, and the improved prediction models for fire spread are detailed in Equations (2) to (6).

$$Uphill: R = R_0 \times K_S \times K_\omega \times K_\phi = 1.0372 \times e^{-0.057m} \times K_S \times e^{0.1783v\cos\theta} \times 0.6172e^{0.0805w} \quad (2)$$

$$Downhill: R = R_0 \times K_S \times K_\omega \times K_\phi = 1.0372 \times e^{-0.057m} \times K_S \times e^{0.1783v\cos(180^\circ-\theta)} \times (0.0249w+1) \quad (3)$$

$$Left-flat-slope: R = R_0 \times K_S \times K_\omega \times K_\phi = 1.0372 \times e^{-0.057m} \times K_S \times e^{0.1783v\cos(\theta+90^\circ)} \quad (4)$$

$$Rigth-flat-slope: R = R_0 \times K_S \times K_\omega \times K_\phi = 1.0372 \times e^{-0.057m} \times K_S \times e^{0.1783v\cos(\theta-90^\circ)} \quad (5)$$

$$Wind-direction: R = R_0 \times K_S \times K_\omega \times K_\phi = 1.0372 \times e^{-0.057m} \times K_S \times e^{0.1783v} \times 0.6172e^{0.0805w} \quad (6)$$

where m is the moisture of the combustibles, v is the wind speed, θ is the angle between the wind direction and the uphill direction, and w is the slope.

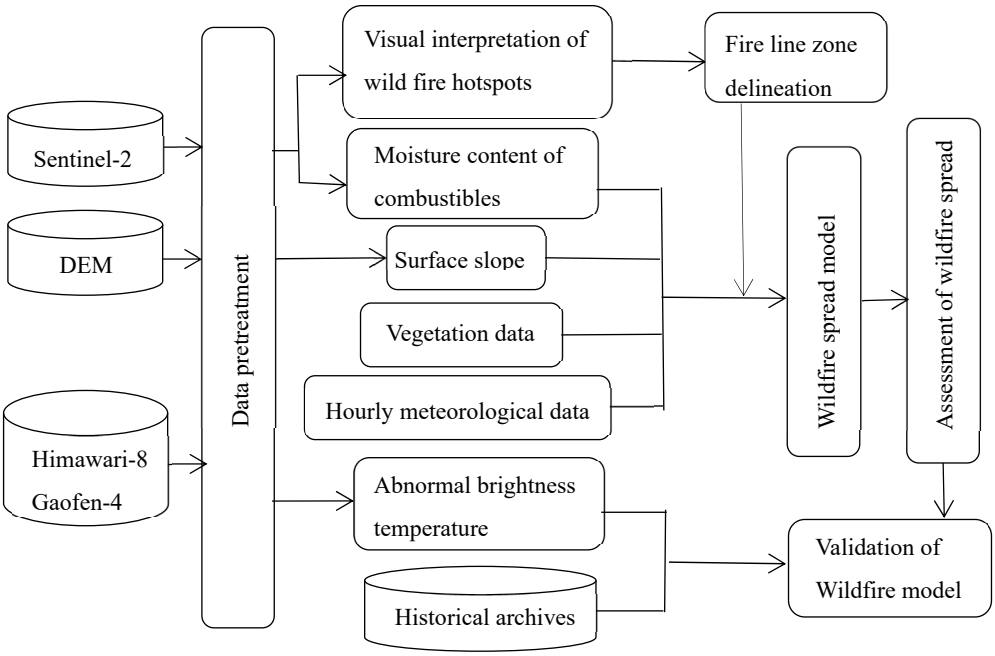


Figure 2. Technical route of forest fire spread simulation based on RS interpretation.

In the models developed by Wang Zhengfei and then improved by others, the temperature effect was not considered, which introduces some limitations to fire spread predictions. As the altitude increases, the temperature in the forest gradually decreases, the relative humidity incrementally increases, and the moisture content of the ground cover also becomes higher, making combustibles less flammable. Additionally, in subalpine zones or near watersheds, precipitation noticeably increases, further reducing the likelihood of forest fires. In mountainous areas, with every 100 m increase in the altitude, the temperature decreases by 0.6 °C [37]. The higher the altitude, the lower the temperature, the greater the relative humidity, the higher the moisture content of the ground cover, and the more significant the increase in precipitation, generally reducing the likelihood of fires.

This paper builds on the abovementioned existing models and incorporates the effects of elevation on fire spread. When calculating the fire spread speed using the models, the combustibles moisture content was based on specific conditions of the selected area and actual satellite RS data obtained at various times during the fire's occurrence and development. Other necessary information for predicting fire spread was also retrieved from the RS data (detailed later on in this paper). It is expected that, by incorporating actual RS data and elevation effects, the prediction of fire spread will be more accurate and reliable.

It has been known that the higher the altitude, the lower the temperature and the higher the humidity or moisture content of the ground vegetation cover, suggesting that the altitude of the forest can affect the fire spread velocity.

The moisture content can affect the initial fire spread speed. Zhang et al. studied the relationship of water content and initial fire spread velocity, which is presented as:

$$R_0 = 1.0372 \times e^{-0.057 \times m}, \quad (7)$$

where m(%) is the moisture content of the combustibles, R_0 (m/min) is the initial spread speed.

Li et al. studied the relationship of the moisture content of ground cover and average temperature, which is:

$$\mathrm{H} = 71.72 - 48.80 \log \mathrm{T}, \quad (8)$$

where H (%) is the water content and T (°C) is the average temperature.

Therefore, by using the equation for the temperature's effect on moisture and how moisture affects the initial fire spread speed, we calculated the relationship between the temperature (which is affected by altitude) and forest fire spread, which is

$$R = 61.84/16.15^{\log T} \quad (9)$$

This section is divided by subheadings. It provides a concise and precise description of the experimental results, their interpretation, as well as the experimental conclusions that can be drawn.

Assuming the initial temperatures of 10, 20, 30, and 40 degrees centigrade, the temperature at different altitudes for each different initial temperature is shown in Table 4.

Table 4. Relationship of elevation and forest fire spread rate.

Elevation (m)	Temperature (°C)	Initial Temperature (°C)			
		10	20	30	40
0	T	0.281	0.649	1.059	1.499
100	T-0.6	0.261	0.625	1.033	1.472
200	T-1.2	0.241	0.602	1.008	1.445
300	T-1.8	0.221	0.579	0.983	1.418
400	T-2.4	0.202	0.556	0.958	1.391
500	T-3.0	0.183	0.533	0.932	1.364
600	T-3.6	0.164	0.511	0.907	1.338
700	T-4.2	0.145	0.488	0.883	1.311
800	T-4.8	0.127	0.466	0.858	1.285
900	T-5.4	0.110	0.444	0.833	1.258
1000	T-6.0	0.093	0.422	0.809	1.232

As shown in Figure 3, the relationship of the fire spread speed and temperature can be expressed as a linear equation:

$$\mathrm{y} = 0.0385\mathrm{x} - 0.0928, \quad (10)$$

where y is the fire spread speed and x is the temperature. Because the temperature decreases by 0.6 °C for each 100 m of elevation increase, as shown in Table 4, the fire spread speed decreases by 0.0231 m/min.

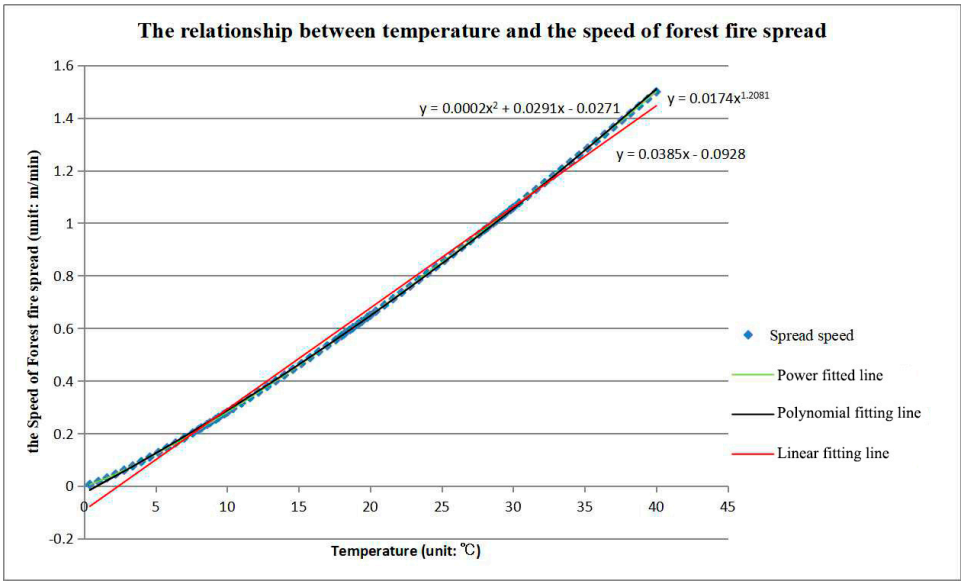


Figure 3. Relationship of temperature and fire spread speed.

Assuming an initial temperature of 25 °C and a spread speed of 0.870 m/min, the speed decreases by 2.7% for every 100 m of elevation. The rate of decrease in the fire spread speed at different initial temperatures is calculated, as shown in Table 5.

Table 5. Fire spread speed reduction at different initial temperatures.

Initial Temperature	Initial Speed of Fire Spread	Reduction in Fire Spread (%)
10	0.292	7.91
15	0.485	4.77
20	0.677	3.41
25	0.870	2.66
30	1.062	2.17
35	1.255	1.84
Average		3.79 ± 2.27

It can be seen in Table 5 that the higher the initial temperature, the slower the reduction in fire spread. And, the improved fire spread model is shown as follows:

$$Uphill: R = R_0 \times K_S \times K_\omega \times K_\phi \times D_{al} = 1.0372 \times e^{-0.057m} \times K_S \times e^{0.1783v\cos\theta} \times 0.6172e^{0.0805w} \times (1 - d_{al} \times h/100) \quad (11)$$

$$Downhill: R = R_0 \times K_S \times K_\omega \times K_\phi \times D_{al} = 1.0372 \times e^{-0.057m} \times K_S \times e^{0.1783v\cos(180^\circ - \theta)} \times (0.0249w + 1) \times (1 - d_{al} \times h/100) \quad (12)$$

$$Left - flat - slope: R = R_0 \times K_S \times K_\omega \times K_\phi \times D_{al} = 1.0372 \times e^{-0.057m} \times K_S \times e^{0.1783v\cos(\theta + 90^\circ)} \times (1 - d_{al} \times h/100) \quad (13)$$

$$Rigth - flat - slope: R = R_0 \times K_S \times K_\omega \times K_\phi \times D_{al} = 1.0372 \times e^{-0.057m} \times K_S \times e^{0.1783v\cos(\theta - 90^\circ)} \times (1 - d_{al} \times h/100) \quad (14)$$

$$Wind - direction: R = R_0 \times K_S \times K_\omega \times K_\phi \times D_{al} = 1.0372 \times e^{-0.057m} \times K_S \times e^{0.1783v} \times 0.6172e^{0.0805w} \times (1 - d_{al} \times h/100) \quad (15)$$

where R is the estimated fire spread speed, R_0 is the initial spread rate, K_s is the combustible material-type correction factor, K_ω is the wind correction factor, K_ϕ is the slope correction factor, D_{al} is the elevation correction factor, m is the moisture content of combustibles, v is the wind speed, θ is the angle between the wind direction and uphill direction, w is the slope, d_{al} is the rate of decrease in the fire spread speed with elevation, and h is the elevation.

Using the fire spread data from ignition experiments conducted by Yu et al. in Kaiyuan, Tieling, and Hengren as the observed values for forest fire spread [35], a comparison was made with the calculated values from the improved model. The correlation coefficient of the model reached 0.9235, an increase of 0.034 compared to the pre-improvement model, indicating that the calculated values from the improved model are closer to the actual observed data.

3.2. Moisture of Combustibles

The methods for estimating vegetation moisture content using optical RS technology generally rely on parameters and models, such as spectral reflectance, vegetation water index, and radiative transfer models. In this paper, the moisture content of combustibles in forest areas was estimated based on spectral analysis and the angle slope index.

The angle slope index included the shortwave angle normalized index (SANI), the shortwave angle slope index (SASI), and the near-infrared angle index (ANIR); initially focused on the three consecutive MODIS bands, NIR, SWIR1, and SWIR2, characterizing their interrelationships; and later introduced the near-infrared angle index (ANIR) (Figure 4 and Equation (16)), characterizing the relationships between the RED, NIR, and SWIR1 bands [24]. The near-infrared angle normalized index (NANI) and the near-infrared angle slope index (NASI) proposed by Deng et al. are shown in Equations (17) and (18), respectively. According to the results of Deng et al., the linear regression model established with the NANI exhibits the highest fit, with a coefficient of determination of 0.791 and an RMSE of 0.047 [23]. We performed fuel moisture inversion based on the linear regression model, with the calculations shown in Equation (19).

$$\mathrm{ANIR}_{(\alpha_{\mathrm{NIR}})} = cos^{-1}\left[\frac{a^2 + b^2 - c^2}{2ab}\right], \tag{16}$$

$$\mathrm{NANI} = \mathrm{ANIR} \times \frac{SWIR1 - RED}{SWIR1 + RED}, \tag{17}$$

$$\mathrm{NASI} = \mathrm{ANIR} \times (\mathrm{SWIR1} - \mathrm{RED}), \tag{18}$$

$$\mathrm{y} = -0.423x + 1.279, \tag{19}$$

where a, b, and c denote the distances, as shown in Figure 4, αNIR is the angle between the RED-NIR and NIR-SWIR1 of the reflectance spectral curve, y is the moisture content of combustibles, and x is the NANI.

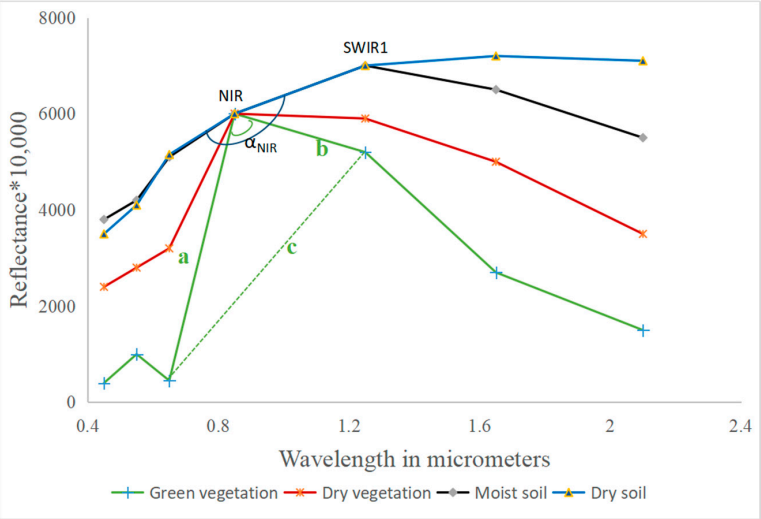


Figure 4. The angle α_{NIR} formed at the NIR by the reflectance at bands red, NIR, and SWIR1. An additive offset was applied to make spectral values equal at the NIR band (adapted from Shruti Khanna et al. [12]).

Here, the moisture content of combustibles in the fireline area was estimated based on ANIR and NANI.

3.3. Slope of the Fire Area

Strictly speaking, the slope at any point on the surface is defined as the angle between the tangent plane passing through that point and the horizontal surface, showing the degree of inclination of the surface at that point. Numerically, it is equal to the angle between the normal vector, $\vec{n}$, of the surface differential element passing through that point and Z. When calculating the slope specifically, a simplified differential formula is commonly used, with the complete mathematical expression being:

$$\text{Slope} = \arctan\sqrt{f_x^2 + f_y^2}, \tag{20}$$

where f_x is the rate of elevation change in the north–south direction, and f_y is the rate of elevation change in the east–west direction. Equation (20) can be used to calculate the slope at a point on the ground, with the key being the calculation of f_x and f_y. Grid DEM represents the terrain surface in a discrete form, and the surface function is generally unknown, so f_x and f_y are typically calculated locally through numerical differentiation methods or local surface fitting methods.

Currently, the mainstream methods for extracting terrain information based on the DEM include six types: the second-order differential method, frame differential algorithm, third-order unweighted differential algorithm, third-order inverse-distance-squared weighted differential algorithm, third-order inverse-distance weighted differential algorithm, and simple differential algorithm [27–29], as shown in Table 6. Among them, the third-order inverse-distance-squared total differential and third-order inverse-distance weighted differential algorithms exhibit the highest accuracy under various statistical indicators. Meanwhile, the simple differential, second-order differential, and frame algorithms show various degrees of bias and extreme cases under different statistical indicators.

Table 6. Mathematical models for the slope and aspect calculations *.

Method of Calculation	f_x	f_y
Simple difference	$(z_5 - z_2)/g$	$(z_5 - z_4)/g$
Second-order difference	$(z_8 - z_2)/(2g)$	$(z_6 - z_4)/(2g)$
Frame difference	$(z_7 - z_1 + z_9 - z_3)/(4g)$	$(z_3 - z_1 + z_9 - z_7)/(4g)$
Third-order unweighted difference	$(z_7 - z_1 + z_8 - z_2 + z_9 - z_3)/(6g)$	$(z_3 - z_1 + z_6 - z_4 + z_9 - z_7)/(6g)$
Third-order inverse-distance weighted difference	$(z_7 - z_1 + 2(z_8 - z_2) + z_9 - z_3)/\left[\left(4 + 2\sqrt{2}\right)g\right]$	$(z_3 - z_1 + 2(z_6 - z_4) + z_9 - z_7)/\left[\left(4 + 2\sqrt{2}\right)g\right]$
Third-order inverse-distance-squared weighted difference	$(z_7 - z_1 + 2(z_8 - z_2) + z_9 - z_3)/(8g)$	$(z_3 - z_1 + 2(z_6 - z_4) + z_9 - z_7)/(8g)$

*: g represents the grid resolution, z_i (i = 1, 2, 3, . . ., 9) represents the elevations of the grid points around the center point, and both f_x and f_y are calculated for each center point [30,38].

In the abovementioned context, the third-order inverse-distance-squared total differential method was selected in this paper, and a 3 × 3 local moving window size was used for the calculation. Table 6 shows the mathematical model for calculating the slope and aspect values.

3.4. Fire Spot Pixel

The Gaofen-4 satellite is capable of performing minute-level, high-frequency, continuous repetitive observations of the same area, and can also rapidly adjust its direction to face the observation area within minutes. Previous research has shown that the optimal detection center wavelength for the spectral characteristics of burning wooden materials is in the range of 3620~4830 nm. Regardless of the presence of visible flames, the mid-infrared imagery from the Gaofen-4 satellite effectively detects high-temperature forest fire spots. The 400 m-resolution mid-infrared imagery can penetrate smoke to identify visible flames. Herein, the mid-infrared channel of Gaofen-4 was used to invert fire spot pixels and to validate the simulation results of the forest fire spread model. An adaptive threshold monitoring algorithm for fire spots, constructed using the "split window method", captures anomalous-brightness temperatures in RS imagery. The specific algorithm is as follows:

A. Calibrate the image's *DN* value to the thermal radiance, $L_e(\lambda_i)$

$$L_e(\lambda_i) = Gain \cdot DN + offset, \tag{21}$$

where $L_e(\lambda_i)$ is the radiance; *DN* is the image grayscale value; *Gain* is the gain coefficient, which represents the proportional relationship between the *DN* and the thermal radiance value; and offset is the absolute calibration coefficient offset value, which is used for adjusting the converted radiation brightness value to ensure that it is closer to the true radiation value.

B. Use the Planck function to solve for the brightness temperature of the star

$$T = \frac{K_{i2}}{\ln(1 + K_{i1}/L_e(\lambda_i))}, \tag{22}$$

where K_{i1} and K_{i2} are constants $K_{i1} = 2h' \times c^2/(\lambda_i^5)$, $K_{i2} = h' \times c/(k \cdot \lambda_i)$, respectively; h' is the Planck constant, 6.626×10^{-34} J · s; c is the speed of light, 2.998×10^8 m/s; and k is the Boltzmann constant, approximately 1.38×10^{-23} J · K^{-1}.

C. Discrimination of fire spot pixels

Combined with the land cover-type map, pixels in the forested area with a brightness temperature greater than 315 K are designated as high-temperature suspect pixels. Set these high-temperature suspect pixels as the center of the initial window, with the initial window size set to 7×7. Calculate the variance and average of the brightness temperature of the background pixels in the window. During the calculation, use the forest NDVI mask operation to exclude other high-temperature suspect pixels from background pixels. If the number of background pixels in the window is less than 20% of the total number of pixels in the window, then expand the window successively to 9×9, 11×11, …, 21×21; if it still does not meet the requirements, abandon the judgment of that pixel and mark it as a non-fire spot pixel. If the suspect pixel meets the conditions of Equation (23), then the pixel is determined to be a fire spot pixel [39].

$$T > T_{bg} + 3\delta T_{bg}, \tag{23}$$

where T_{bg} is the average brightness temperature of the background pixel, δT_{bg} is the standard deviation, T_{bg}.

The Himawari-8 satellite was equipped with the advanced imager AHI. The temporal resolution of the entire observation area is 10 min, and the spatial resolution of the mid-infrared image is 2 km (channel 7) [40]. According to Planck's law, the difference in the radiation brightness results shows that, even if the fire area only accounts for 1/104~1/103 of the total area of the pixel, the brightness temperature value of the fire point pixel in the mid-infrared band significantly increases, and there is a significant difference compared to the surrounding pixels. In the far-infrared band, this difference in the brightness temperature also occurs, but the difference is smaller. This characteristic of bright temperature

difference can be used as the basis for fire point identification. The method of discriminating the fire point pixel of the algorithm in this study is as follows [13]:

Daytime: The pixels that meet the conditions {A or [B and C and D and (E or F)]} are recognized to be a fire; otherwise, they are non-fire spots.

Night: The pixels that meet the conditions [A or (B and C and D)] are recognized to be fire spots; otherwise, they are non-fire spots.

A: $T7 > 360K(Night320K)$

B: $\Delta T > \Delta\overline{T} + 3.5\delta_{\Delta T}$

C: $\Delta T > \Delta\overline{T} + 6K$

D: $T_7 - \overline{T}_7 > 2\delta_7$

E: $T_{14} - \overline{T}_{14} > 2.5\delta_{14}$

F: $\delta'_7 > 5K$

In the formula, T_7 and T_{14} are Himawari-8 data (3.9 μm and 11.2 μm, respectively) channel temperatures. $\overline{T}_7$ and $\overline{T}_{14}$ are the average temperatures of 3.9 μm and 11.2 μm, respectively in the background window. ΔT is the temperature difference between 3.9 μm and 11.2 μm. $\Delta\overline{T}$ is the average temperature difference between 3.9 μm and 11.2 μm in the background window. δ_7 and δ_{14} are the temperature standard deviations of 3.9 μm and 11.2 μm, respectively, in the background window. $\delta_{\Delta T}$ is the standard deviation of the temperature difference between 3.9 μm and 11.2 μm in the background window. δ'_7 is the 3.9 μm standard deviation of the fire spot pixel in the background window.

4. Results

4.1. Visual Interpretation of Forest Fire Hotspots

Visual interpretation is based on high-resolution imagery, its 3D stereoscopic images, and verified historical interpretation experience. The true-color images from Sentinel-2 have a spatial resolution of 10 m, clearly revealing smoke from the fire spots. The false-color images, with a spatial resolution of 20 m, allow a clear observation of burning fire areas. The 3D stereoscopic images enable interpretations to intuitively distinguish between valleys, slopes, and mountain tops, allowing for the correct identification of uphill, downhill, left and right slopes, and wind direction, and providing important information for subsequent forest fire spread predictions.

Forest fire hotspots are typical abnormal characteristics produced by the burning of forest vegetation, including fire spots and smoke spots. Fire spots refer to the visible flames in the vegetation burning process, while smoke spots are locations where a large amount of smoke is formed due to the evaporation of the vegetation's own moisture during combustion. Using 10 m optical satellite imagery during a fire, true-color (bands 4, 3, and 2) and false-color (bands 12, 11, and 8A) combinations, along with information on vegetation cover and regional topography (slopes, valley lines, and ridge lines), the visual interpretation markers for the hotspots and key fire areas was achieved.

From the true-color composite image of the Mianning 4.24 forest fire (Figure 5), it can be seen that the fire area is covered by a large area of smoke. The smoke starts at the smoke point and spreads out in a band-like extension along the wind direction, gradually changing in color from dark gray to light gray. The shape is continuously distributed in a "broom-like" fashion, and it can be distinguished from cloud-covered areas based on the shape, color, and the shadows of the clouds, clearly differentiated from the surrounding dark-green background.

From the false-color composite image of the Mianning 4.24 forest fire (Figure 6), it can be seen that the fire line emerges under the smoke cover along the ridge lines and windward slopes, appearing as strip-shaped. Fire spots intermittently appear along the fire line, appearing as bright red in the composite image. Burned areas appear dark brown and are "L"-shaped, distinctly differentiated from the surrounding blue vegetation and light-yellow non-forested areas.

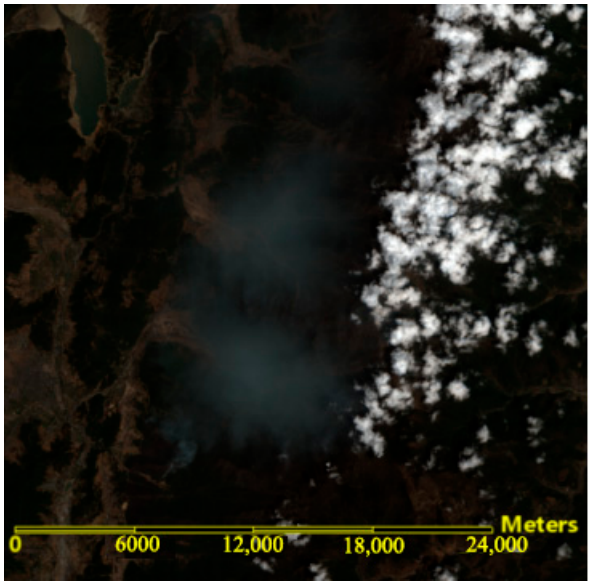


Figure 5. True-color composite image of the Mianning 4.24 forest fire.

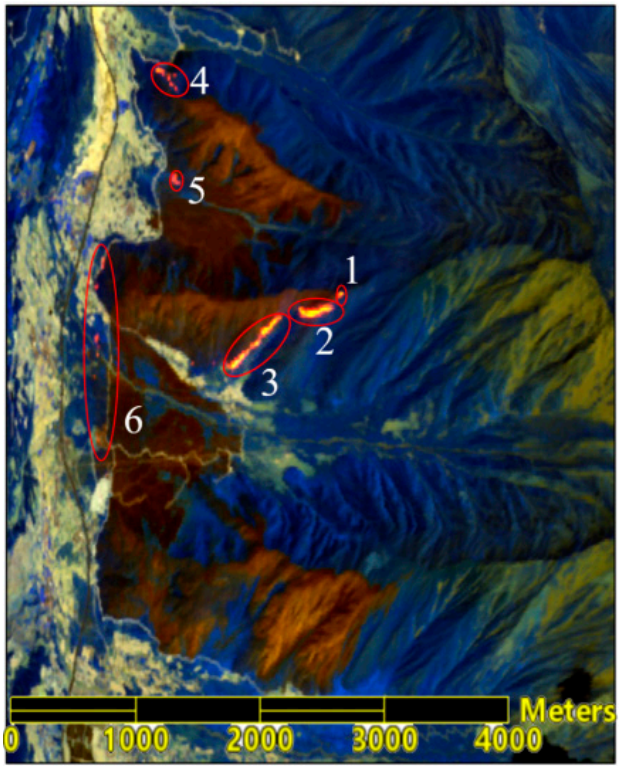


Figure 6. False-color composite image of the Mianning 4.24 forest fire (numbers 1–6 are the range of fire lines).

By integrating the DEM data, the remote sensing image of the forest fire area was visualized in 3D, combined with the regional topography (slopes, valley lines, and ridge lines). Six areas were identified, as shown in Figure 7. Among these, areas 1, 2, and 3 are located on the eastern side of the fire site, on the ridge, and on the sun-facing slopes, respectively, where the fire is more intense; areas 4, 5, and 6 are located on the western side of the fire site, at the base of the mountain (valley line), and on the shaded slopes, respectively, where the fire is less intense.

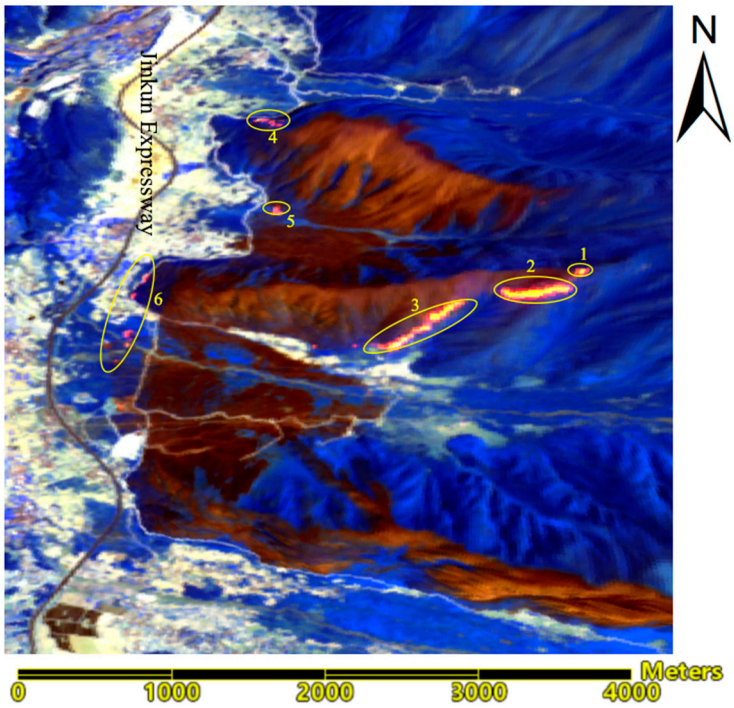


Figure 7. Three-dimensional visualization of the fire scene (numbers 1–6 are the range of fire lines).

4.2. Moisture of Combustibles

Based on spectral analysis and the angle slope index, the moisture content of combustibles in the fire area can be determined by using the multispectral remote sensing data from Sentinel-2's Band 4, Band 8, and Band 11. Additionally, based on the normalized difference vegetation index (NDVI), vegetation cover in the fire area can be obtained using Band 4 and Band 8, and the results after error correction are shown in Figure 8. The results of the moisture content of combustibles, overlaid with vegetation cover data masks to remove background environmental impacts, are shown in Figure 9. After excluding outliers, the average moisture content is 0.583 $\pm$ 0.145, the minimum and maximum values being 0.013 and 1.355, respectively. Values below 0.357 account for 1.5% and values between 0.362 and 0.795 account for 89.2%, with the moisture content concentrated between 0.388 and 0.682, accounting for 77.7%. Pixels near the fire line, affected by the intensity of the fire, mostly have a moisture content ranging from 0 to 0.232, with the highest moisture content in adjacent areas exceeding 1. According to Li et al., the same type of vegetation has a higher moisture content in the undergrowth and the canopy layer due to the physiological moisture of sprouting new leaves and branches, while ground cover has a lower moisture content due to the influence of dead leaves and branches, and it varies significantly with the weather conditions [41]. In this study, the canopy vegetation moisture content inverted using Sentinel-2 should be higher than the actual moisture content of combustibles; however, this deviation should converge due to the high temperatures and smoke at the fire scene.

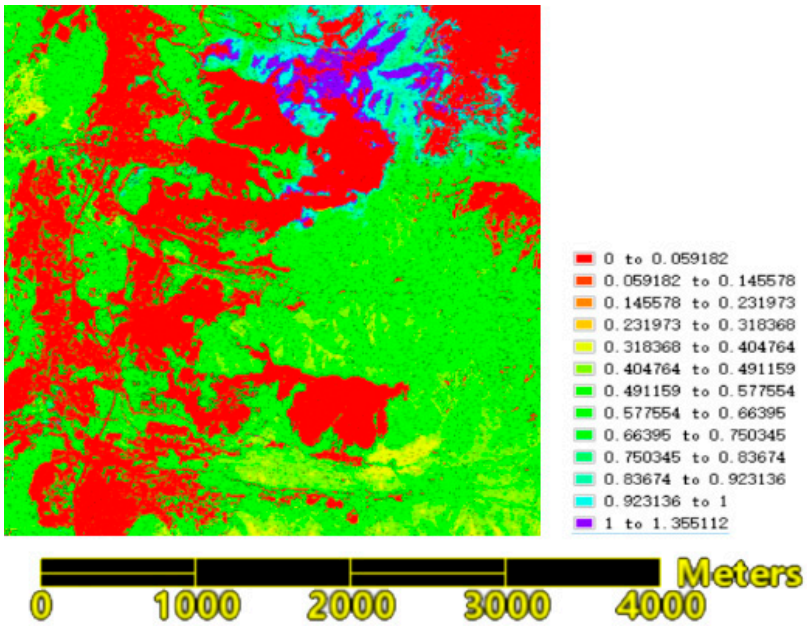


Figure 8. Normalized vegetation index after error correction.

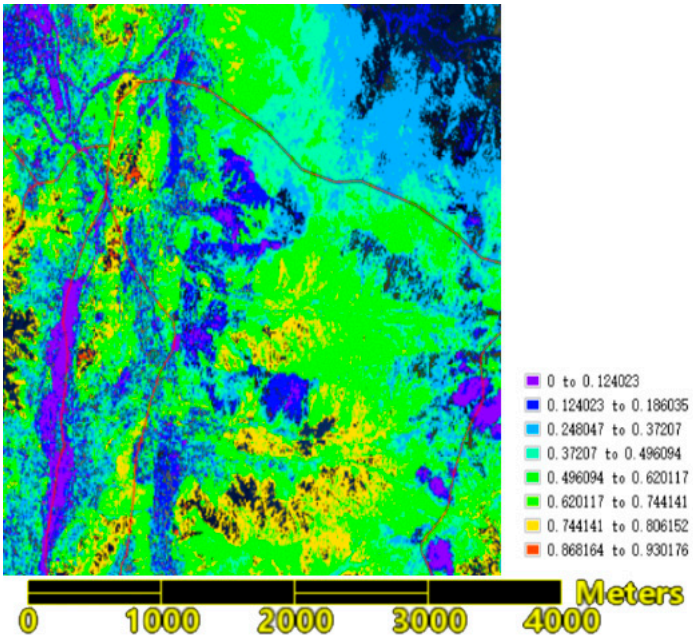


Figure 9. The estimated moisture content in combustibles.

4.3. Slope Data from the DEM

The third-order inverse-distance-squared total differential method with a 3 × 3 local moving window size was used to compute the 30 m STER GDEM data. The results are shown in Figure 10. From the interpreted statistical data, the minimum and maximum values are 0.0049 and 88.76, respectively, and the average slope value is 24.19 ± 15.36, with a high standard deviation. The high standard deviation is most likely due to the fire area featuring high mountains, steep slopes, less gentle slopes, and obvious relief features. There are 267,043 pixels with slopes ranging from 0 to 59 degrees, accounting for 99.4% of the total, and 1668 pixels with slopes between 80 to 88.76 degrees, accounting for 0.6%.

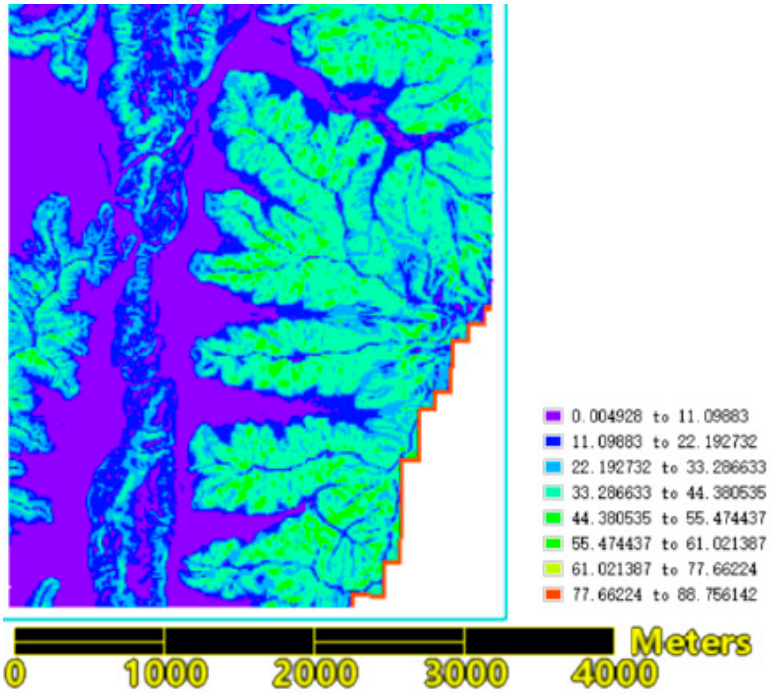


Figure 10. Result of slope extraction from the DEM.

4.4. Wind Speed

Wind factors are divided into wind direction and wind speed. Generally, the wind direction is the direction of the fire front's spread and the wind speed directly affects the spread speed of the fire. The higher the wind speed, the faster the fire spreads in the direction of the wind and the higher the wind speed correction factor [42]. On 24 April 2021 at T04:00:00 Z, the wind speed was 1.44 m/s to the north and −0.78 m/s to the east (or 0.78 m/s to the west), resulting in an actual wind direction from the northwest with a wind speed of 1.638 m/s, forming an angle of 241.56 degrees in the uphill direction. The correction factors for wind force in various directions are shown in Table 7.

Table 7. Correction factors of wind force in all directions.

Uphill	Downhill	Leftward	Rightward	Wind Direction
$e^{0.1783v\cos\theta}$	$e^{0.1783v\cos(180-\theta)}$	$e^{0.1783v\cos(\theta+90^\circ)}$	$e^{0.1783v\cos(\theta-90^\circ)}$	$e^{0.1783v}$
0.870	1.149	1.293	0.774	1.339

4.5. Correction Factor for Combustible Materials

Although a combustible material correction factor, K_S, was considered in Wang Zhengfei's model for fire spread prediction, detailed classifications of combustible material types were unavailable, which makes precise calculations difficult, if not impossible [43]. Zheng developed an empirical constants table for the impact factors of combustible material types [44], as shown in Table 8.

According Tang et al. [45], the fire area is mostly primary forest, with the vegetation cover exceeding 80%, predominantly consisting of broadleaf forests, such as eucalyptus. Secondary forests are typically dominated by broadleaf species, have mixed stand structures, and include a mixture of trees and shrubs. By comparing this with the types of combustibles listed in Table 8, the type of combustibles in the fire scene area is most similar to the secondary forest listed in the table. Therefore, the correction factor of 0.7, corresponding to the secondary forest in the table, is taken as the combustible-type correction factor for the fire spread prediction.

Table 8. Correction coefficient (K_S) of combustible types for forest fire spread speed.

Combustible Type	Correction Factor K_S	Combustible Type	Correction Factor K_S
Coniferous forest	0.4	Secondary forest	0.7
Flat pine needles	0.8	Red pine, Yunnan pine, and Huashan pine	1.0
Dead branches and fallen leaves	1.2	Thatch grass and weeds	1.6
Sedge and dwarf birch	1.8	Pasture grassland	2.0

4.6. Prediction of RS-Enabled Fire Spread

The slope and terrain are key factors affecting the speed of wildfire spread. Typically, fires spread slower downhill and faster uphill. The steeper the slope, the easier it is for water to run off, making the combustibles drier and indirectly accelerating the spread of the fire. This also affects the moisture content of the combustibles: sunlit slopes receive more sunlight, making the combustibles less moist and more flammable; conversely, combustibles on shaded slopes retain more moisture, making them less flammable. Therefore, based on the three-dimensional visualization of the fire scene (Figure 7), the positions of different fire lines on uphill, downhill, left-level slopes, right-level slopes, as well as the wind direction, were determined. Targeted fire speed simulations for each direction were also conducted.

As shown in Figure 7, the north wind direction coincides with the direction of the left-level slope and the east wind (which is negative) coincides with the downhill direction. The actual wind direction is from the northwest. Because burned areas generally do not reignite and form a barrier, they are not included in predictions for fire spread speeds. On the eastern line, sectors 1, 2, and 3 have intense fires and are located on uphill terrain with steep slopes, leading to faster spread speeds. Therefore, the fire spread speeds for uphill land, left-level slope, and-right level slope at the top of the fire line in sector 1 are predicted, while for the fire lines in sectors 2 and 3, the spread speeds for uphill and right-level slope directions are predicted. For the fire line in sector 4, which is at the base of the mountain, with a relatively low slope, the fire spread speeds for uphill land, left-level slope, downhill, and wind direction are predicted. Other fire spread predictions include downhill and wind direction for sector 5, and downhill, left-level slope, right-level slope, and wind direction for sector 6.

After incorporating the remote sensing data and temperature effects associated with different elevations, the prediction results are as follows:

In the Fire Line 1 area, there are 15 adjacent pixels, with one outlier removed. The vegetation moisture content is below 0.01, with the minimum and maximum slopes being 13.24 degrees and 42.34 degrees, respectively. The maximum speeds for uphill, left-level slope, and right-level slope are 11.782, 0.939, and 0.562 m/min, respectively.

In the Fire Line 2 area, there are 32 adjacent pixels, with one outlier removed. Five pixels have a vegetation moisture content below 0.01, with the maximum reaching 1.008. The slopes are above 34.5 degrees, with the maximum slope being 45.01 degrees. The maximum fire spread speeds in the uphill and right-level slope directions are 13.858 and 0.562 m/min, respectively.

In the Fire Line 3 area, there are 55 adjacent pixels, with five outliers removed. Nineteen pixels have a vegetation moisture content below 0.01, while the majority of the remaining pixels is around 0.5, with the highest value reaching 0.911. The minimum slope is 15.500 degrees and the maximum slope is 46.544 degrees. The maximum fire spread speeds in the uphill and right-level slope directions are 16.527 and 0.562 m/min, respectively.

In the Fire Line 4 area, there are 26 adjacent pixels, with nine pixels with a moisture content below 0.01, and the rest between 0.483 and 0.987. The slopes are above 33 degrees,

with the maximum slope being 41.770 degrees. The maximum speeds for uphill, left-level slope, downhill, and wind direction are 11.254, 0.939, 1.702, and 17.319 m/min, respectively.

In the Fire Line 5 area, there are nine adjacent pixels, with a moisture content between 0.5 and 0.6. The slopes range from 11.984 degrees to 12.550 degrees. The maximum downhill speed is 1.061 m/min and the maximum wind direction speed is 1.587 m/min.

In the Fire Line 6 area, there are 47 adjacent pixels, with one outlier removed. Ten pixels have a vegetation moisture content below 0.01, and the rest between 0.415 and 0.733. The slopes are below 28 degrees, with the minimum slope being 1.024 degrees. The maximum fire spread speeds for downhill, left level slope, right level slope, and wind direction are 1.378, 0.939, 0.562, and 5.669 m/min, respectively.

Given the limitations of time and spatial resolution values associated with satellite RS images, the sudden nature of forest fires, and the accuracy of RS inversion parameters, the fire spread range one hour later is based on the statistical values of forest fire spread speed results in each direction mentioned above. The results are shown in Table 9 and Figure 11.

Table 9. Maximum spread distance after 1 h in all directions with RS (unit: meter).

Location of Fire Line	Uphill	Left	Right	Downhill	Wind Direction
Zone 1	706.91	56.31	33.70		
Zone 2	831.47		33.70		
Zone 3	991.62		33.70		
Zone 4	675.25	56.31		102.13	17.32
Zone 5				63.67	95.22
Zone 6		56.31	33.70	82.69	340.14

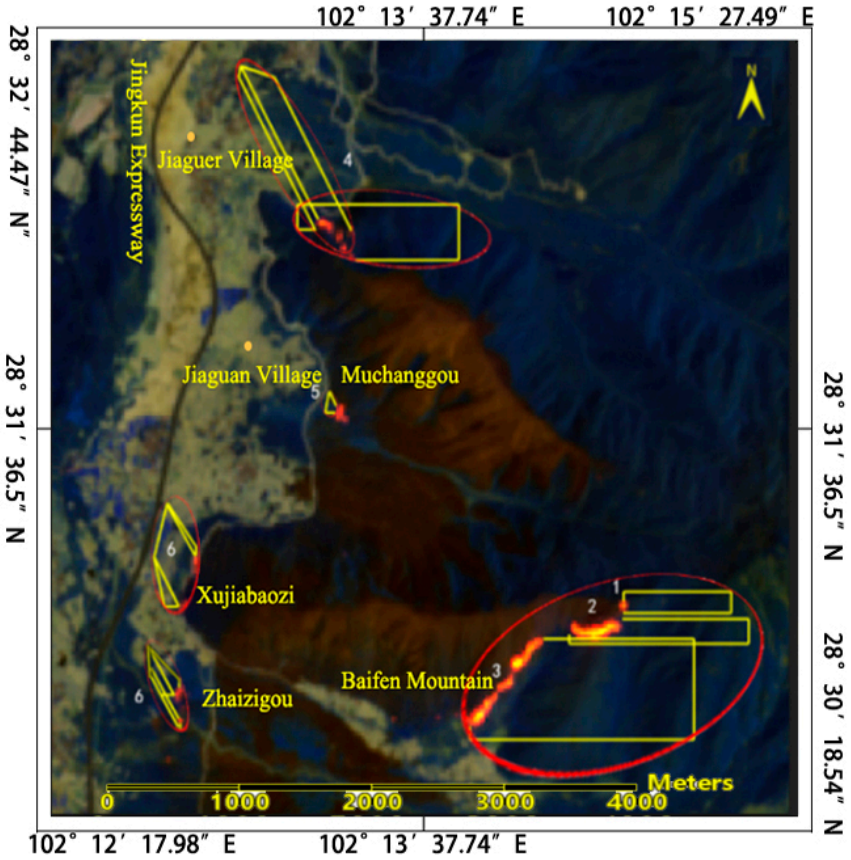


Figure 11. Prediction of fire line spread distance one hour later.

It is evident that the fire spread speed is the fastest in the uphill direction, resulting in the longest spread distance, while the spread distances on the left-level slope and the right-level slope are essentially the same. Note that Fire Line 6 shows a greater spread distance in the wind direction.

The RS-enabled fire spread prediction can provide critical information for firefighters to effectively combat fires. In the case of the Mianning fire, based on the land cover-type map before the forest fire (from the National Basic Geographic Information Center) (as shown in Figure 11) and high-resolution remote sensing imagery (Sentinel-2), the west side of the forest fire borders the Jingkun Expressway (as shown in Figures 12 and 13), which is non-forested and forms a barrier. Typically, a forest fire extinguishes on its own upon encountering non-combustible materials, unless spot fires occur (which cause the fire to jump to other mountain tops). Therefore, based on the RS-enabled fire spread prediction, it is recommended that defense and firefighting efforts should concentrate on eastern sectors 1, 2, and 3, as well as the northern and eastern areas of sector 4 on the western line.

4.7. Prediction of Fire Spread by the Improved Forest Fire Spread Model Without RS (Conventional Fixed-Point Predictions)

The forest fire spread prediction results from the traditional model were used to compare accuracy values with the predictions from the RS model. The calculation process follows Equations (11) to (15), where the value of m is derived from meteorological data for relative humidity. The relative humidity and initial temperature values are shown in Table 3. The elevation and slope values are taken from the relative center point of the fire line area for the calculations. The simulation results are shown in Table 10.

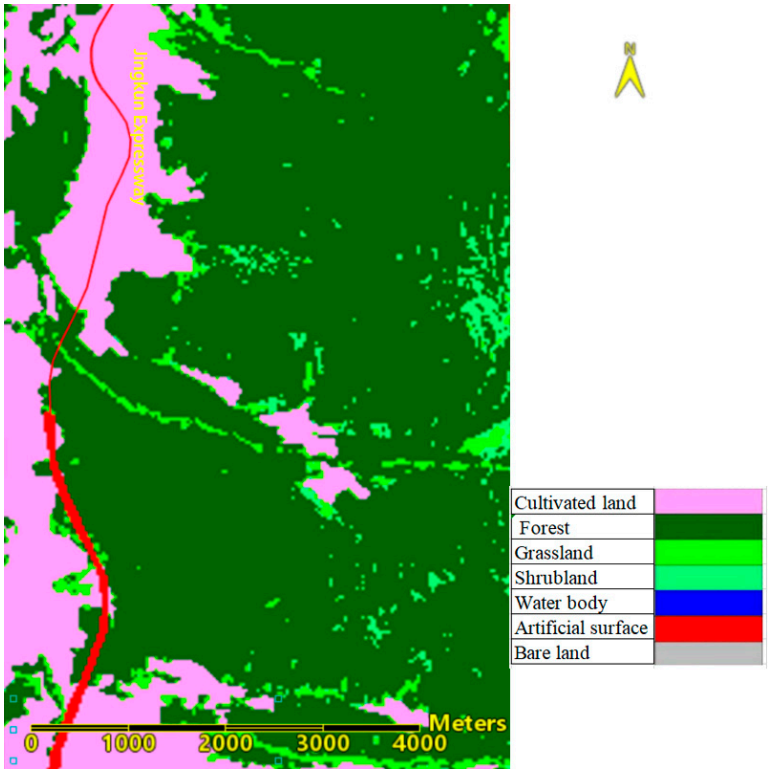


Figure 12. Fire area land cover-type map.

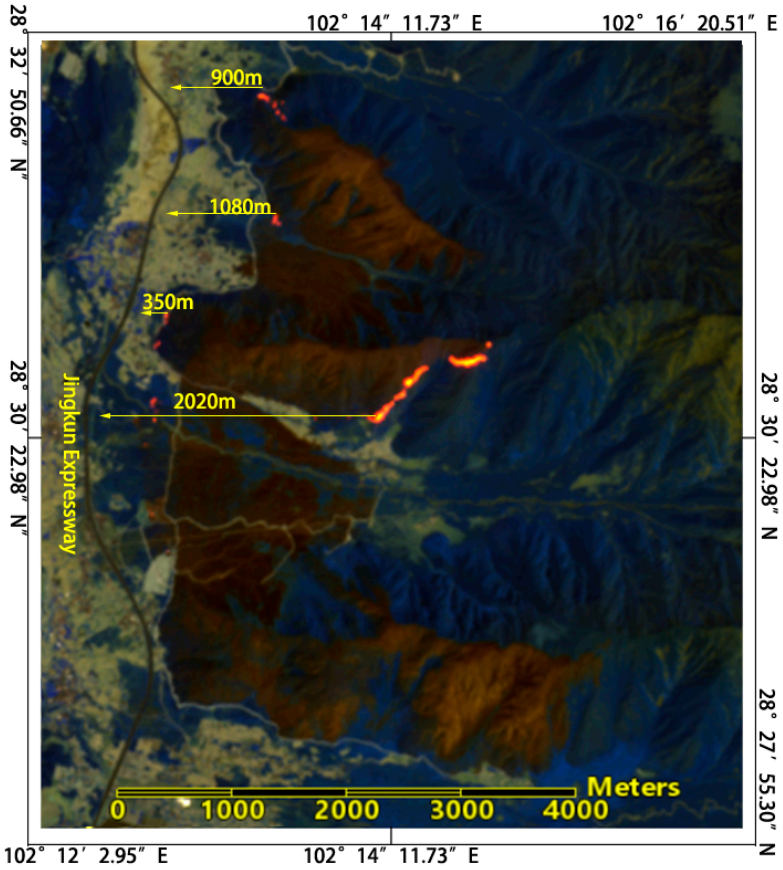


Figure 13. Map of the fire line and Jingkun Expressway locations.

Table 10. Maximum spread distance after 1 h in all directions without RS (unit: meter).

Location of Fire Line	Uphill	Left	Right	Downhill	Wind Direction
Zone 1	267.06	54.46	32.59		
Zone 2	586.98		32.59		
Zone 3	972.02		32.59		
Zone 4	575.52	54.46		96.88	885.67
Zone 5				63.51	95.37
Zone 6		54.46	32.59	123.17	123.17

As shown in Table 10, the spread distance in the downhill direction in Zone 6 and in the wind direction in Zone 4 show a much larger increase compared to the RS-enabled fire spread model simulations, with an abnormal increase in the wind direction. In contrast, the spread distances in other directions for the fire line were smaller than those predicted by the RS-enabled model. The abnormal increase in the wind direction in Zone 4 may be attributed to the center point selected for the prediction having a slope significantly greater than the statistical values from remote sensing inversion.

4.8. Comparison of RS-Enabled Fire Spread Prediction to the Actual Mianning Fire

According to the hourly meteorological data for Mianning County on 24 April 2021, shown in Table 3, between T4:00 and 5:00, the wind direction and speed changed from north at 1.44 m/s and east at −0.78 m/s to north at 1.48 m/s and east at −0.54 m/s, indicating relatively stable conditions. Based on the maximum spread distances in each direction, shown in Table 9, the average increase in the visible fire area was calculated to be 3.257 hm^2/10 min (square hectare per 10 min) within one hour. The analysis of

the dynamic changes in the visible fire area of the Mianning forest fire monitored by the Himawari-8 satellite every 10 min from 24 April 2021 T03:40 to 24 April 2021 T05:00 (UTC) (Figure 14) shows a significant increase in the visible fire area, with an average increase rate of 3.297 hm^2 per 10 min. This rate can be considered consistent with the results achieved by the RS-enabled forest fire spread model. The small discrepancy may be likely due to the differences in the spatial resolution between remote sensing images. The traditional forest fire spread simulation model predicted an average increase in the open flame area of 3.5637 hm^2 per 10 min. This shows a significant discrepancy when compared to the actual monitoring results.

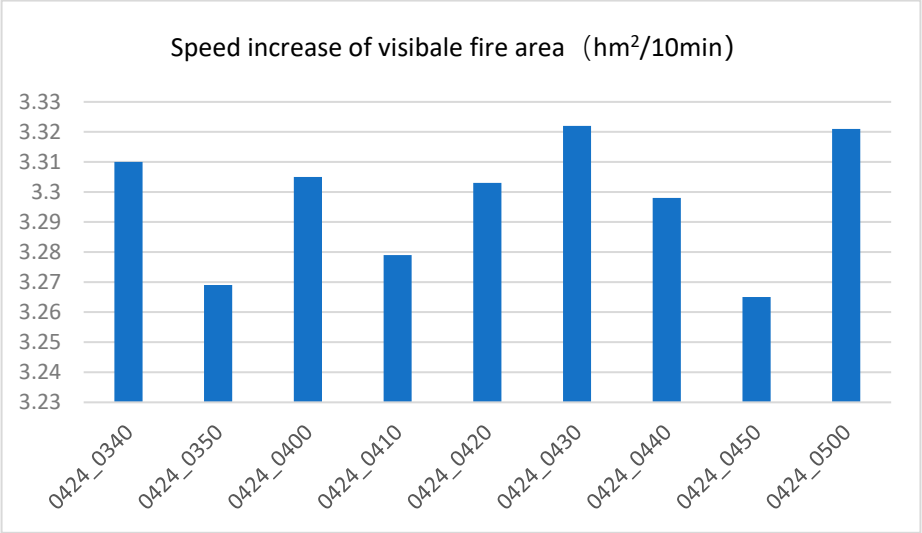


Figure 14. Dynamic map of the increase in the visible fire area at the Mianning 4.24 forest fire site monitored by the Himawai-8 satellite.

According to the analysis of the remote sensing imagery of fire spots from the Himawari-8 satellite on April 24 from 3:40 to 5:00 (Figures 14 and 15), the fire monitoring points progress westward from Jiaguan Village and do not cross the Jingkun Expressway (102°12′38″ E). It extended eastward from Baifen Mountain and northward from Dashuigou (as shown in rectangles 1, 2, 3, and 4 in Figure 16), consistent with the trend observed in the forest fire spread model simulations.

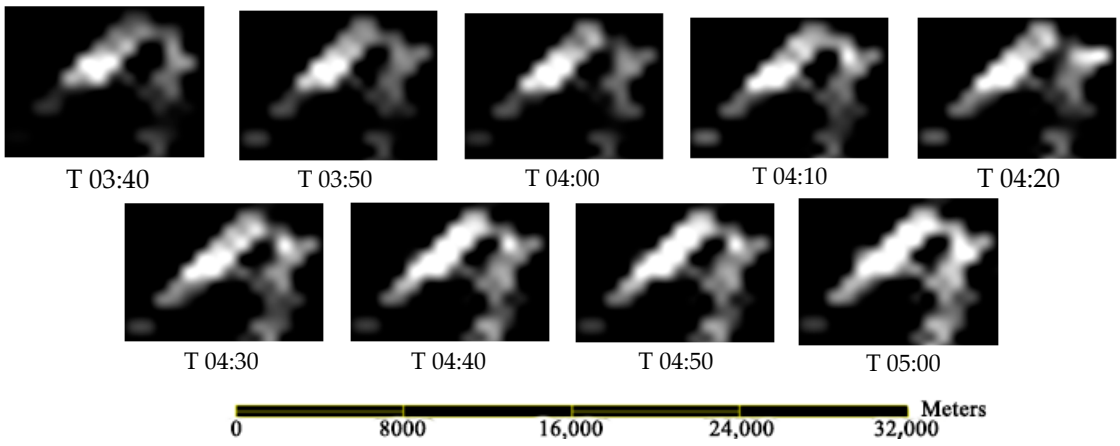
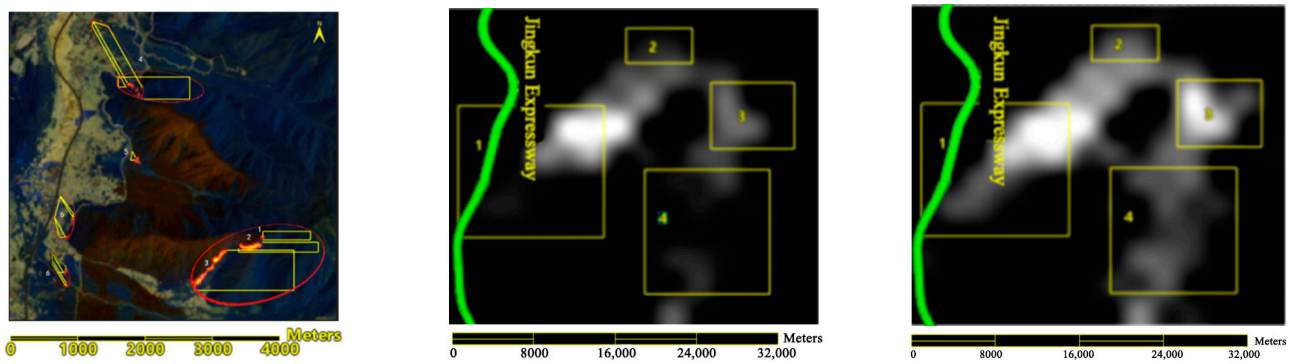


Figure 15. Himawari-8 remote sensing imagery brightness temperature anomaly monitoring results from 24 April 2021 T03:40 to 24 April 2021 T05:00.



(**a**) (**b**) (**c**)

Figure 16. Comparison of forest fire spread model simulation results and remote sensing monitoring. (**a**) Forest fire spread simulation results; (**b**) Himawari-8 remote sensing imagery brightness temperature anomaly monitoring at T03:40; (**c**) Himawari-8 remote sensing imagery brightness temperature anomaly monitoring at T05:00. (The green line is the Jingkun Expressway; the yellow line is the comparison region).

Using the mid-infrared image from Gaofen-4 IRS, taken 58 min after the Sentinel-2 image at T03:45, the anomaly temperature perception in the forest fire area was studied to verify the results of the RS-enabled forest fire spread data. The Gaofen-4 data were collected at 04:43:42 on April 24, and the brightness temperatures derived from the mid-infrared band are shown in Figure 17. Using the 20 m resolution remote sensing image from Sentinel-2 as a base image, the Gaofen-4 infrared IRS image was geometrically corrected and precisely registered. The two images were overlaid with the Gaofen image on top, with the top image's transparency being set to 50%, as shown in Figure 18. Upon enlargement, the boundary of the anomaly temperature and the predicted forest fire spread area overlapped, as shown in Figure 19. The results clearly show that the predicted forest fire spread area (regions 1–6) essentially aligns well with the brightness temperature anomaly boundary detected by the Gaofen-4 IRS image. The small discrepancies may have been caused by factors such as smoke from the fire, lower mid-infrared image resolution, and firefighting activities.

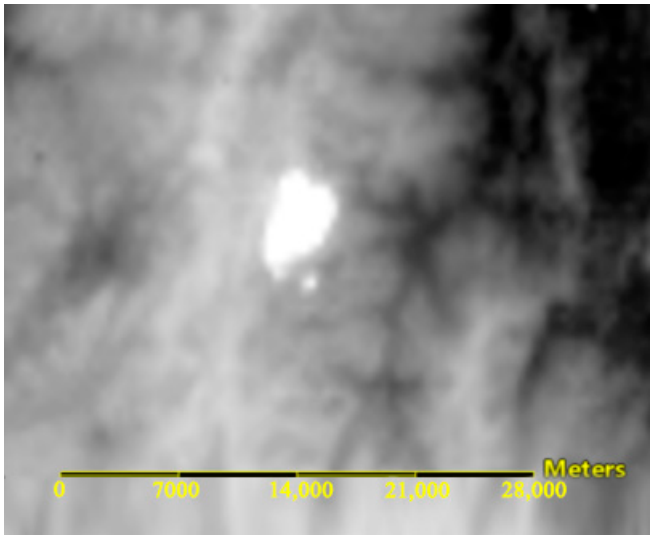


Figure 17. Gaofen-4 mid-infrared brightness temperature map.

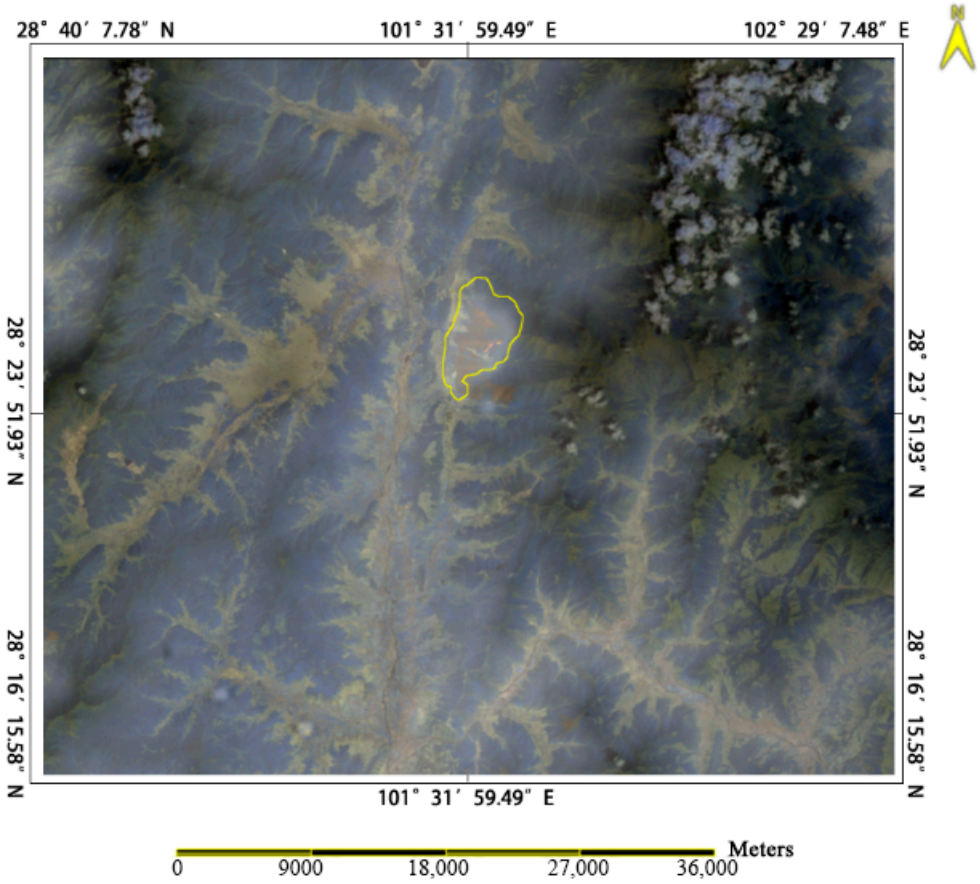


Figure 18. Gaofen-4 mid-infrared brightness temperature map (the yellow indicates the boundary of the abnormal brightness temperature).

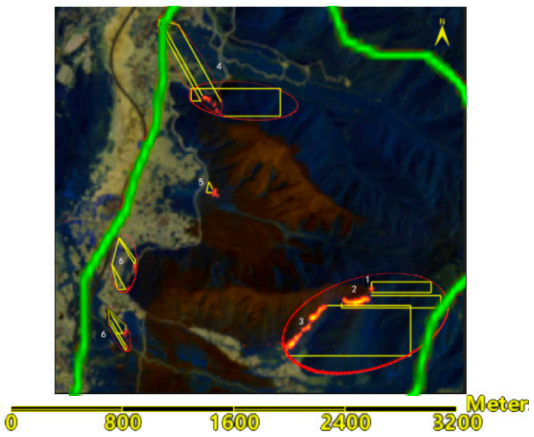


Figure 19. Overlaid results of the abnormal brightness temperature boundary and the predicted forest fire spread area (the green line indicates the abnormal brightness temperature boundary; the yellow line indicates the forest fire spread area).

The deduced spread area is also consistent with the results of Tang et al.'s research [44] and historical archives.

The analysis above shows that the predicted spread area of the model generally matches the actual spread results, demonstrating the accuracy and reliability of the RS-enabled fore fire spread model for predicting forest fire development, particularly in fires occurring in difficult-to-access areas.

5. Discussion

Traditional forest fire spread models often rely on fixed-point measurements, rough estimates, or substituting similar values for parameter assignments due to the difficulty of obtaining field parameters, and thus lead to less accurate predictions. The large-scale static parameters used by Wang Zhengfei in his improved model do not effectively reflect the small- and medium-scale changes in real forest fires, which are crucial to accurately predict the speed of fire spread. In contrast, RS-enabled fire prediction models can retrieve, sometimes in real time, remote sensing data from fire scenes and invert the key parameters required for the fire spread model. The small- and medium-scale changes in real forest fires are included in the high-resolution remote sensing data, and the parameters used in the RS-enabled model are statistical values derived from remote sensing interpretations, which can better reflect the actual conditions of the entire fire scene and, thus, result in simulation outcomes that are closer to the real values.

Take as an example the improved Wang Zhengfei model by Tian et al. (2024) [46], which was based on the NDVI (normalized vegetation index) value inverted from Landsat-8 satellite data and combined with cellular automata to predict the forest fire spread in Muli County, Sichuan Province, China, in 2020. The NDVI was used to introduce vegetation density to improve the Wang Zhengfei fire spread model, which is insensitive to changes in fuel density. However, due to the significant influence of the moisture content in a combustible forest, a higher NDVI does not necessarily mean that the forest fire spread speed will increase proportionally. The cellular automaton applied the same evolution rules in all directions and ignored the differences in local environments in various directions, thus leading to the fire line simulation exhibiting a tendency toward uniformity. The prediction results show an area error rate of 58.81%, which is quite high. By comparing the prediction results of the method proposed by Tian et al. with the RS-enabled forest prediction model proposed in this paper, it can be seen that the RS-enabled model can more accurately predict forest fire spread and can better represent the actual forest fire spreading process in terms of the fire area—the results from the monitoring and RS-enabled prediction models are consistent, with 3.297 hm^2 per 10 min for monitoring and 3.257 hm^2 per 10 min for the prediction. In addition, the fire ground boundary can also be simulated more accurately with the RS-enabled model. These improvements may be attributed to the following factors: (1) the evolutionary rules of cellular automata result in a relatively uniform trend in fire line inference, while actual fire lines may only significantly spread in one or two directions, often leading to inconsistent accuracy in practical applications; (2) compared to the NDVI of combustibles, the humidity factor of combustibles plays a more important role in the spread prediction model; and (3) a better grid spatial resolution (the maximum spatial resolution of Sentinel-2 data is 10 m) and the optimization of humidity index extraction improved the prediction accuracy of the RS-enabled model.

Although the RS-enabled fire prediction model captured the actual fire field boundary to some extent, there is still a gap in the results when compared to the actual complex fire spread boundary. In addition, the model still performs relatively poor in certain areas, such as the top right of the fire scene in the Mianning fire. Such a poor performance in certain areas is likely attributed to the following reasons: (1) to evaluate the potential maximum harm or damage by forest fires, the study used the maximum of the statistical values in each direction to calculate the spread area of forest fires; (2) the change in the wind direction caused by the rugged terrain formed a unique environment inside the fire site and local climatic phenomena affected the prediction; (3) the limitations in data collection also led to the inability to accurately capture local microclimate data; and (4) the model did not take into account human intervention measures, such as isolation belts set by fire fighters, which would further increase the prediction error.

In future research, improvements should be made in the following areas:

(1) In response to the phenomena of flying fire and direction change in the fire line caused by the change in the wind field induced by heat exchange during combustion, the

WRF (Weather Research and Forecasting) model [47] can be included in the forest fire spread model.

(2) Regarding the different small-scale fire environments, the area within the scope of the fire can be subdivided further, and detailed statistics can be determined for each small area. Meanwhile, the spread rate of a forest fire can be predicted for a more, different time points, which can further improve the simulation accuracy, though it may be limited by the acquisition of remote sensing images. Note that the high-spatial-resolution remote sensing images have a low temporal resolution and the high-temporal-resolution remote sensing images have a low spatial resolution. If the advantages of both the high-spatial-resolution and the high-temporal-resolution remote sensing images can be integrated, the RS-enabled fire prediction model proposed in this paper will be greatly improved.

(3) Given the limitations of the time and spatial resolution of remote sensing satellite imagery, which prevent the real-time acquisition of forest fire imagery data, future research should employ techniques, such as super-resolution image reconstruction, pixel unmixing, and sub-pixel analysis, to enhance the spatial scale of high-temporal-resolution data. Additionally, more efficient image registration techniques can be used to improve the accuracy of the inversion location. Incorporating key factors, such as the surface temperature and combustible biomass that affect the speed of fire spread, can also benefit forest fire predictions. Additionally, studying RS collection methods for these influencing factors across different satellite data is expected to further enhance the model's applicability. As a crucial component of intelligent forest fire management, advanced RS technology is expected to further enhance the accuracy and precision of forest fire predictions.

6. Conclusions

The spread speed of forest fires is a crucial factor for predicting forest fire behavior. Many factors influence the spread speed. This study examines the impact of temperature changes at different altitudes on the spread speed, with the model correlation coefficient reaching 0.92. This indicates that the altitude significantly affects the initial spread speed of forest fires and can be an important factor for estimating the spread speed. Additionally, this study obtained parameters required for the forest fire spread model by retrieving Sentinel-2 RS images of a forest fire: The moisture content of combustibles in the forest area were inverted based on spectral analysis and the angle slope index. Slope data were calculated using the third-order inverse-distance-squared full difference method and using a 3×3 local moving window size, based on the DEM. Fire spot detection during the forest fire was conducted using both Himawari-8 and Gaofen-4 satellite data and served as a basis for evaluating the accuracy of the fire spread model simulation results.

This study simulates forest fire spread using the example of the Mian County forest fire in Sichuan Province. The results show: (1) The fire line in the Baifen Mountain area is located on a sunny slope, with fuel moisture content in most of the adjacent areas below 0.01, and the slope mostly above 34.5 degrees, with a maximum elevation of 46.5 degrees. The fastest spread is uphill, reaching 16.5 m/min. (2) In Jiaguer Village, also on a sunny slope, one-third of the adjacent pixel points have a moisture content below 0.01, with the remainder around 0.5, and the slope exceeding 33 degrees, with a maximum elevation of 41.8 degrees. The wind direction creates the fastest spread rate, reaching 17.32 m/min. (3) The fire line in Muchanggou is located in a valley near the mountain foot, with the moisture content between 0.5 and 0.6, an average slope of 12 degrees, and a maximum spread rate of only 1.59 m/min, in the wind direction. (4) The fire lines in Xujiabaozi and Zhaizigou are located near the mountain foot, adjacent to a road. One-fifth of the pixel points have a moisture content below 0.01, with the remainder ranging from 0.41509 to 0.73250, with a minimum slope of just 1 degree. The maximum spread rate in the wind direction reaches 5.67 m/min. (5) Across the entire fire line area, the average increase in the open flame area within one hour is 3.257 hm^2/10 min.

The analysis of the dynamic changes in the visible fire area of the Mianning forest fire, monitored by the Himawari-8 satellite at 10 min intervals from 03:40 to 05:00 on 24 April 2021, showed an average increase in the visible fire area of 3.297 hm^2 per 10 min, which is consistent with the results simulated by the RS-enabled forest fire spread mode (3.257 hm^2 per 10 min). The conventional fixed-point prediction model for forest fire spread estimates an average fire area growth rate of 3.5637 hm^2/10 min, which shows a significant discrepancy compared to the Himawari-8 satellite monitoring results. Based on the mid-infrared images from Gaofen-4 IRS, taken 58 min after the Sentinel-2 image, to identify the anomaly temperature in the forest fire area, the results of the forest fire spread were validated. The results show that the predicted forest fire spread area aligns well with the brightness temperature anomaly boundary detected by the Gaofen-4 IRS images. The dual validation results show that the spread area deduced by the RS-enabled forest fire spread model in this study generally matches the actual spread results and can serve as a basis for assessing the fire situation.

The continuous advancement of satellite remote sensing interpretation technology can effectively address the challenges of obtaining the necessary parameters for forest fire spread prediction models and the poor universality of algorithms. In the future, more key factors regarding forest fire spread could be inverted using remote sensing imagery from different sensors with varying spatial and temporal resolutions. Using RS-enabled forest fire prediction models to deduce the trends of forest fire spread is expected to effectively enhance the scientific basis for fire assessment and proactive defense planning.

Author Contributions: Conceptualization: G.Z. and P.L.; methodology, study data collection, formal analysis, and writing—original draft: P.L.; funding acquisition and writing—review, comments, and editing: G.Z. All authors have read and agreed to the published version of the manuscript.

Funding: This research was funded by a project supported by the Scientific Research Fund of Hunan Provincial Education Department under grants 23B0244 and 22A0194, the Science and Technology Innovation Platform and Talent Plan Project of Hunan Province under grant 2017TP1022, the Natural Science Foundation of Hunan Province under grant 2024JJ7645, and the Field Observation and Research Station of Dongting Lake Natural Resource Ecosystem, Ministry of Natural Resources.

Data Availability Statement: The data presented in this study are available upon request from the corresponding authors. The data are not publicly available due to our lab's policies or confidentiality agreements.

Acknowledgments: We thank the Department of Emergency Management of Hunan Province for their provision of the forest fire hotspot data.

Conflicts of Interest: The authors do not have conflicts of interest regarding this study.

References

1. Cai, W.; Yang, J.; Liu, Z.; Hu, Y.; Liu, S.; Jing, G.; Zhao, Z. Forest regeneration and its influencing factors in the burnt areas of Daxing'anling Forest Region, Heilongjiang Province. *Acta Ecol. Sin.* **2012**, *32*, 3303–3312.
2. He, W.; Bai, J. Application and prospects of the Canadian Forest Fire Behavior Prediction System. *World For. Res.* **2014**, *3*, 82–86.
3. Sun, X.; Fan, W.; Li, M. Study and implementation of forest fire spread models. *For. Mach. Woodwork. Equip.* **2009**, *5*, 16–19.
4. Zhang, J.; Liu, B. Prediction of fire behavior of mixed combustibles on the forest floor of Pinus koraiensis and Quercus mongolica under flat and windless conditions using the generalized Rothermel model. *Chin. J. Appl. Ecol.* **2012**, *6*, 1495–1502.
5. Wang, Z. Measurement method for the initial spread rate of wildfires. *Mt. Res.* **1983**, *1*, 42–51.
6. Dozier, J. A method for satellite identification of surface temperature fields of subpixel resolution. *Remote Sens. Environ.* **1981**, *11*, 221–229. [CrossRef]
7. Flannigan, M.D.; Vonder Haar, T.H. Forest fire monitoring using NOAA satellite AVHRR. *Can. J. Forest Res.* **1986**, *16*, 975–982. [CrossRef]
8. Flasse, S.P.; Ceccato, P. A contextual algorithm for AVHRR fire detection. *Int. J. Remote Sens.* **1996**, *17*, 419–424. [CrossRef]
9. Giglio, L.; Descloitres, J.; Justice, C.O.; Kaufman, Y.J. An enhanced contextual fire detection algorithm for MODIS. *Remote Sens. Environ.* **2003**, *87*, 273–282. [CrossRef]
10. Mao, K.; Qin, Z.; Liu, W. MODIS image and single-window algorithm are used to retrieve land surface temperature in the Bohai Rim region. *Geomat. Spat. Inf. Technology.* **2004**, *6*, 23–25.

11. Ding, L.; Qin, Z.; Mao, K. Research and parameter determination of split-window algorithm based on MODIS image data. *Remote Sens. Technol. Appl.* **2005**, *2*, 284–289.
12. Qin, X.; Zhu, X.; Yang, F.; Zhao, K.; Pang, Y.; Li, Z.; Li, X.; Zhang, J. Tiangong-1 hyperspectral data detection of fire state sensitive spectrum analysis. *Spectrosc. Spectr. Anal.* **2016**, *33*, 1908–1911.
13. Giglio, L.; Schroeder, W.; Justice, C.O. The collection 6 MODIS active fire detection algorithm and fire products. *Remote Sens. Environ.* **2016**, *178*, 31–41. [CrossRef]
14. Li, G.; Kong, X.; Liu, F.; Lian, M. "Gaofen-4" satellite remote sensing technology innovation. *Spacecr. Recovery Remote Sens.* **2016**, *37*, 7–15.
15. Li, J.; Chen, H.; Li, K.; Dou, X.; Zhao, H.; Zeng, J.; Zhang, X.; Qian, Y. Urban surface temperature inversion and its application with domestic high resolution thermal infrared data. *Remote Sens. Nat. Resour.* **2024**, *8*, 1–9.
16. Karagianni, A.C.; Lazaridou, M.A. Remote sensing techniques in monitoring areas affected by forest fire. In Proceedings of the Fifth International Conference on Remote Sensing and Geoinformation of the Environment (RSCy2017), Paphos, Cyprus, 20–23 March 2017; Volume 28, pp. 3255–3269.
17. Shi, Y.; Shan, H.; Zhang, Y.; Hu, M. Research on forest fire monitoring of new generation of geostationary meteorological satellite. *For. Fire Prev.* **2017**, *4*, 32–35.
18. Xu, H.; Zhang, G.; Zhou, Z.; Zhou, X.; Zhou, C. Forest fire monitoring and positioning improvement at subpixel level: Application to himawari-8 fire products. *Remote Sens.* **2022**, *14*, 2460. [CrossRef]
19. Li, Z.; Ma, H.; Tang, B.; Duan, S.; Zhou, C.; Leng, P.; Zhao, W.; Liu, X.; Shang, G.; Chen, K.; et al. *GB/T 43997.2-2024*; Thermal Infrared Remote Sensing Inversion of Land Surface Temperature—Part 2: Split Window Method. National Remote Sensing Technology Standardization Technical Committee (SAC/TC 327): Beijing, China, 25 April 2024.
20. Jiang, B.; Chen, T.; Zhang, L.; Feng, Z.; Wei, B. Study on forest fire spread model based on remote sensing interpretation. *China Emerg. Rescue* **2021**, *3*, 11–16.
21. Charles, W.R.; Dudley, W. Lambert Absorption Coefficients of Water in the Infrared. *J. Opt. Soc. Am.* **1971**, *10*, 1316.
22. Carter, G.A. Primary and Secondary Effects of Water Content on The Spectral Reflectance of Leaves. *Am. J. Bot.* **1991**, *78*, 916–924. [CrossRef]
23. Deng, B.; Yang, W.; Mu, N.; Zhang, C. Study on vegetation water content based on spectral analysis and angle slope index. *Spectrosc. Spectr. Anal.* **2016**, *36*, 2546–2552.
24. Khanna, S.; Palacios-Orueta, A.; Whiting, M.L.; Ustin, S.L.; Riaño, D.; Litago, J. Development of angle indexes for soil moisture estimation, dry matter detection, and land-cover discrimination. *Remote Sens. Environ. Interdiscip. J.* **2007**, *109*, 154–165. [CrossRef]
25. Tucker, C.J. Remote sensing of leaf water content in the near infrared. *Remote Sens. Environ.* **1980**, *10*, 23–32. [CrossRef]
26. Lei, J.; Yang, W.; Yang, X.; Li, H. Vegetaion Canopy Moisture Inversion based on Improved Distance Projection Ratio Index. *People's Yangtze River* **2021**, *52*, 113–118.
27. Liu, X. Analysis and Evaluation of Error in Rule Grid Digital Elevation Model Interpretation Algorithms. Master's Thesis, Wuhan University, Wuhan, China, 2002.
28. Tang, G.; Yang, Q.; Zhang, Y.; Liu, X. Accuracy of ground slope extraction from DEMs at different scales—A test in the loess hilly gully region. *Bull. Soil Water Conserv.* **2001**, *21*, 53–56.
29. Liu, X.; Gong, J.; Zhou, Q.; Tang, G. Analysis of accuracy of DEM slope and aspect algorithms. *J. Surv. Mapp.* **2004**, *33*, 258–263.
30. Hao, Z. Comparison of DEM slope and aspect algorithms under different terrains. *Hydropower and Energy Science* **2011**, *29*, 68–70.
31. Chen, N.; Wang, Q. Analysis of the application range of 6 slope extraction algorithms—A study in the loess hilly gully region. *Mapp. Inf. Eng.* **2006**, *31*, 20–21.
32. Li, F.; Li, J.; Zhang, Q. Comparative study of DEM slope and aspect extraction algorithms. *Anhui Agric. Sci.* **2008**, *36*, 7355–7357.
33. Jiang, J.; Li, Y.; Wang, Y. Comparative analysis of 6 slope extraction algorithms based on DEM—A case study of Qingdao City, Shandong Province. *Mapp. Spat. Geogr. Inf.* **2018**, *41*, 195–199, 206.
34. Ministry of Emergency Management of the People's Republic of China. *Ten Typical Cases of National Emergency Rescue in 2021 Were Released*; People.cn: Beijing, China, 2022.
35. Mao, X.; Xu, W. Study on calculation methods for forest fire spread rate. *Liaoning Meteorol.* **1991**, *1*, 9–13.
36. Zhang, X.; Liu, P.; Wang, X. Research on the improvement of Wang Zhengfei's forest fire spread model. *Shandong For. Sci. Technology* **2020**, *50*, 1–6, 40.
37. Fan, J.; Gao, J. *Middle School Geography (First Semester of The Seventh Grade)*, 1st ed.; People's Education Press: Beijing, China, 2012; p. 56.
38. Sharpnack, D.A.; Akin, G. An algorithm for computing slope and aspect from elevations. *Photogramm. Eng.* **1969**, *35*, 247–248.
39. Liu, S.; Li, X.; Qin, X.; Sun, G.; Liu, Q. Adaptive threshold segmentation of ignition points in GF-4 PMI images. *J. Remote Sens.* **2020**, *24*, 215–225.
40. Roberts, G.J.; Wooster, M.J. Fire detection and fire characterization over Africa using Meteosat SEVIRI. *IEEE Trans. Geosci. Remote Sens.* **2008**, *46*, 1200–1218. [CrossRef]
41. Li, C. Study on the relationship between forest fuel moisture content and fire risk level. *Yunnan For. Investig. Plan.* **1994**, *4*, 37–42.
42. Mao, X. The effect of wind and terrain on the spread speed of forest fires. *J. Appl. Meteorol.* **1993**, *1*, 100–104.
43. Xue, H.; Hu, X. Exploiting Sensor Spatial Correlation for Dynamic Data Driven Simulation of Wildfire. In Proceedings of the ACM/IEEE/SCS Workshop on Principles of Advanced and Distributed Simulation (PADS), Zhangjiajie, China, 15–19 July 2012.

44. Zheng, H. Calculation and application of fire field parameters. *Agric. Press* **1988**, *4*, 8–9.
45. Tang, Y.; Wang, L.; Deng, C.; Gan, Y.; Zhao, J. High-resolution remote sensing technology assists in emergency firefighting and hidden hazard prediction of forest fires—A case study of the "4·20" forest fire in Mianning. *J. Remote Sens.* **2021**, *25*, 2015–2026.
46. Tian, Y.; Jin, C.; Wang, B.; Li, M. Forest fire spread prediction based on improved Wang Zhengfei model combined with cellular automata. *J. Cent. South Univ. For. Technol.* **2024**, *44*, 14–25.
47. Li, C.; Meng, Q.; Cui, W. Impact of dynamic wind flow behavior on forest fire spread using WRF Model: A case study of "3.30" forest fire in Xichang. *Sci. Technol. Eng.* **2023**, *23*, 4579–4585.

Disclaimer/Publisher's Note: The statements, opinions and data contained in all publications are solely those of the individual author(s) and contributor(s) and not of MDPI and/or the editor(s). MDPI and/or the editor(s) disclaim responsibility for any injury to people or property resulting from any ideas, methods, instructions or products referred to in the content.